Chapter 20

X-ray Magnetic Circular Dichroism: A Primer for Chemists

Stephen P. Cramer

Department of Applied Science, EU 111, University of California, Davis, CA 95616

X-ray **m**agnetic **c**ircular **d**ichroism – XMCD – is the difference in absorption of left- and right-circularly polarized x-rays by a magnetized sample. Although MCD with x-rays is only about 15 years old, the physics is essentially the same as for UV-visible MCD that has been known since 1897. For (bio)inorganic chemists and materials scientists, XMCD has the advantage of elemental specificity that comes with all core electron spectroscopies. Thanks to simple sum rules, XMCD can provide quantitative information about the distribution of spin and orbital angular momentum. Other strengths include the capacity to determine spin orientations from the sign of the XMCD signal, to infer spin states from magnetization curves, and the ability to separate magnetic and non-magnetic components in heterogeneous samples. With new synchrotron radiation sources and improved end stations, XMCD measurements on biological samples are, if not routine, at least no longer heroic. One goal of this review is to encourage chemists, materials scientists, and biologists to consider XMCD as an approach to understanding the electronic and magnetic structure of their samples.

In Paramagnetic Resonance of Metallobiomolecules; Telser, J.;
ACS Symposium Series; American Chemical Society: Washington, DC, 2003.

Introduction

X-ray magnetic circular dichroism, XMCD [1], measurements compare the relative absorption of left- and right-circularly polarized [2] x-rays by magnetized samples (**Figure 1**). Circularly polarized x-rays have oscillating electric and magnetic fields that are 90 degrees out of phase (**Equation 1**). We use the convention of Born and Wolf [1], in which the instantaneous electric field E_{rcp} for a right circularly polarized photon propagating in the z direction resembles a right-handed screw (**Figure 1**).

$$\vec{E}_{rcp} = E_0\{\sin[\omega t - kz + \phi_0]\mathbf{i} + \cos[\omega t - kz + \phi_0]\mathbf{j}\} \qquad (1)$$

In this equation, ω is the angular frequency, $\omega = 2\pi\nu$, k is the wave number, $k = 2\pi/\lambda$ where λ is the wavelength, ϕ_0 is an arbitrary phase shift, and **i** and **j** are unit vectors along the x and y axes respectively. With the above definition, it turns out that left circularly polarized photons carry $\hbar$ angular momentum.

Although the Born and Wolf convention is standard for optics and chemistry literature, most physics literature uses the opposite definition, and one should check how the polarization is defined if the sign of the MCD effect is to be meaningful. The papers of deGroot and Brouder generally use the Born and Wolf convention, while those of Thole, van der Laan, and Carra use the physics or 'Feynman' definition [2]. The pitfalls of describing circular polarization have been cogently described by Kliger *et al.* [3].

In 1690, Huygens discovered that either of the two light rays refracted by a calcite crystal could be extinguished by rotation of a second 'analyzer' crystal [4]. One evening, more than a century later (1808), Malus observed that sunlight reflected from a window pane had similar properties, and by analogy with magnetic bodies, he called this light 'polarized' [5]. Although these early observations were first interpreted in terms of Newton's 'corpuscular' theory [6], by the 1820's Fresnel had developed the mathematical foundation for polarized light in terms of two perpendicular transverse waves [7]. In 1846, Faraday demonstrated rotation of the plane of polarization induced by a magnetic field [8,9]. This 'Faraday effect' or 'magnetic optical rotation' is the result of circular birefringence – which is a difference in the real part of the index of refraction for left and right circular polarization. Prompted in part by these results, the theoretical work of Maxwell completed the picture of light as an electromagnetic wave [10].

The first demonstration of a magnetically induced difference in absorption (the imaginary part of the complex index of refraction) came with the Nobel prize-winning work of Zeeman [2]. After first observing both linear and magnetic circular dichroism in the sodium D emission lines in a magnetic field

In Paramagnetic Resonance of Metallobiomolecules; Telser, J.;
ACS Symposium Series; American Chemical Society: Washington, DC, 2003.

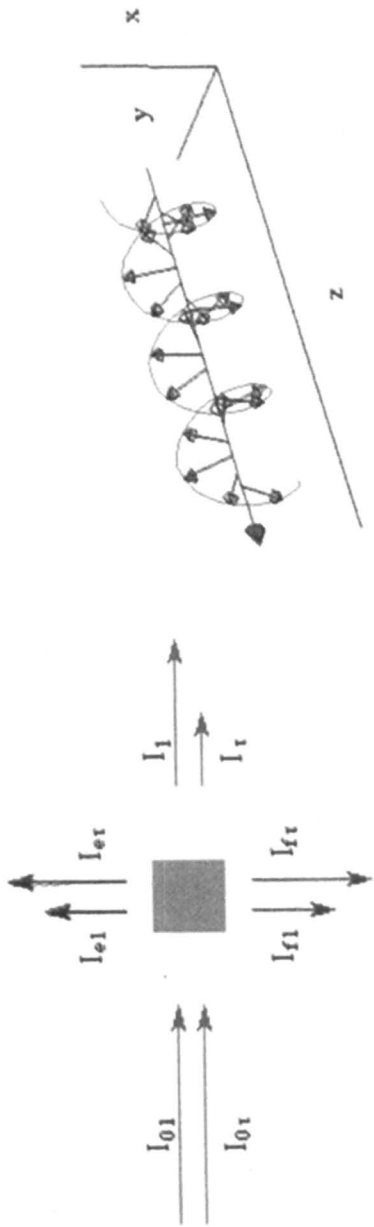

Figure 1 – (Left) Schematic of XMCD experiment. I_{0r} and I_{0l} are respectively the incident beam intensities for rcp and lcp x-rays, and I_r and I_l are the transmitted intensities. The remaining arrows correspond to rcp and lcp electron or fluorescence yields. (Right) Illustration of the electric field direction along the propagation axis for right circularly polarized light.

[11], he reversed the experiment and observed MCD effects on the D absorption lines of Na vapor [12]. After the discovery of x-rays by Röntgen in 1895 [13], attempts were made to observe magnetic effects on x-ray spectra [14,15]. However, a successful experiment would have to wait another 80 years. The modern history of XMCD begins with Erskine and Stern predicting a magneto-optical Kerr effect (MOKE) for ferromagnetic Ni at the $M_{2,3}$ edge ($3p \rightarrow 3d$) [16]. Subsequent attempts to see XMCD in a GdFe alloy at the Gd L_3 edge were unsuccessful [17]. A year later, Thole, van der Laan, and Sawatzky predicted strong XMCD and x-ray magnetic linear dichroism (XMLD) in the $M_{4,5}$ ($3d \rightarrow 4f$) edges of rare earths [18], and the latter was reported in 1986 [19]. The XMCD effect was finally observed at the K-edge of metallic Fe by Schütz and coworkers in 1987 [20]. A much stronger soft x-ray MCD at the Ni $L_{2,3}$ edge was reported in 1990 [21] (**Figure 2**). Our group reported the first XMCD for a paramagnetic metalloprotein in 1993 [22]. Since then, the growth of XMCD for materials science applications has been explosive [23], leading to more than 1000 papers over the past decade.

Experimental Considerations

"In principle therefore all polarization experiments which are possible with visible light can be performed with x-rays. ... it is in practice difficult to obtain sufficient intensity"
Skalicky and Malgrange, 1972 [24]

The key ingredients for an XMCD measurement include (1) a source of circularly polarized x-rays, (2) a monochromator and optics (a 'beamline'), (3) a means for producing a magnetized sample, and (4) an x-ray absorption detection system. Items (3) and (4) are considered the 'endstation'.

Sources of Circularly Polarized X-Rays

Before the introduction of synchrotron radiation beamlines, sources of circularly polarized high energy photons were exotic, such as magnetically oriented radioactive nuclei [25,26] and astronomical synchrotron radiation [27]. Although the concepts behind x-ray circular polarizers had been demonstrated with Cu Kα radiation [28], the resultant beams were not bright enough (~15 photons/sec) for practical applications.

Bend Magnets. The bend magnets associated with particle storage rings are the simplest sources of circular polarization. By viewing the electron (or positron) beam off-axis, one observes a charge accelerated in an elliptical orbit, while viewing the beam on-axis reveals only a horizontal component to the acceleration (**Figure 3**). Thus, the synchrotron radiation emitted from bend magnets is highly polarized – ranging from pure linear polarization in the plane

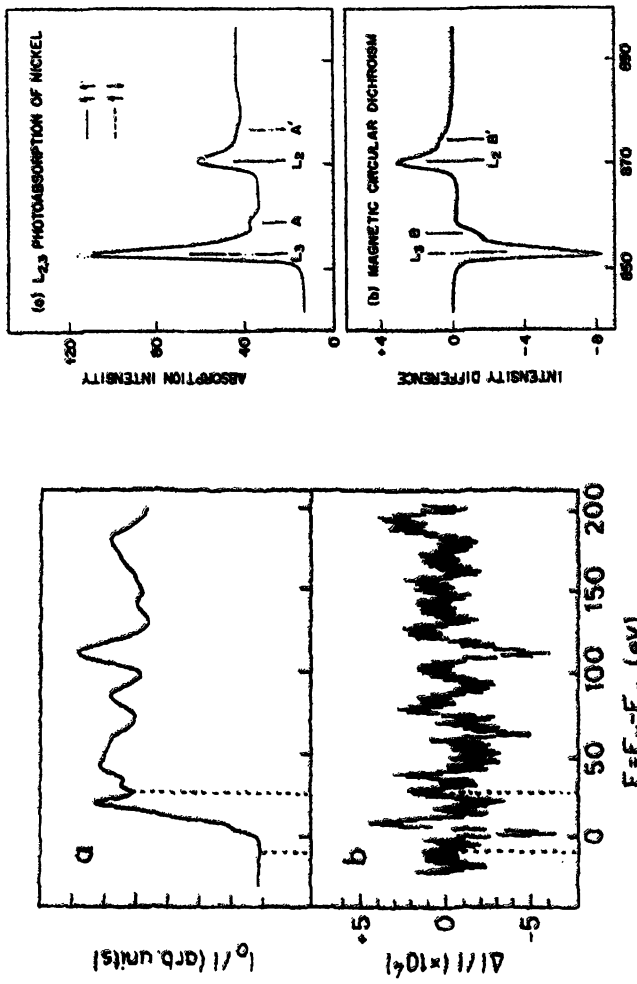

Figure 2 – The first Fe K-edge XANES and EXAFS (different scales) XMCD spectrum, from Schütz et al. [20]. (Right) The first soft x-ray MCD spectrum, reported for Ni metal by Chen and coworkers [21].

of the orbit to nearly circular far out of the plane. Borrowing from Kim [29], the relative amplitudes of the horizontal and vertical electric field components (E_x and E_y) are given by **Equation 2**:

$$\begin{pmatrix} E_x \\ E_y \end{pmatrix} = \begin{pmatrix} K_{2/3}(\eta) \\ \dfrac{i\gamma\psi\ K_{1/3}(\eta)}{\sqrt{1+(\gamma\psi)^2}} \end{pmatrix} \qquad (2)$$

where $K_{1/3}$ and $K_{2/3}$ are modified Bessel functions, y is the ratio of photon energy to the critical energy, γ is the ratio of the electron energy to its rest mass energy, and $\eta = (y/2)\ [1+ (\gamma\, y)^2]^{3/2}$. Defining r as the ratio of the minor to major axes of the polarization ellipse, given by $r = E_y / iE_x$, yields the degree of circular polarization P_c (defined as P_3 by Kim): $P_c = 2r/(1+r^2)$ [29].

Although bend magnets can provide any desired degree of polarization, this comes at a price – the flux falls dramatically as ψ increases. The strongest XMCD is obtained with pure circular polarization, but as $P_c \rightarrow 1$, $I \rightarrow 0$. One therefore has to make a tradeoff between flux and polarization. A figure of merit for most XMCD experiments is P^2I, and the angle for optimal P^2I depends on the photon energy and the critical energy of the ring (**Figure 3**). Apart from limited P_c, other drawbacks of bend magnets are modest brightness and the emission of lcp and rcp in different directions. Better XMCD measurements can be done with insertion device beamlines.

Insertion devices. Insertion devices are magnetic structures 'inserted' into straight sections of the storage ring lattice to produce synchrotron radiation with special characteristics. Although other insertion devices, such as asymmetric wigglers, crossed undulators, and helical undulators [30,31] are sometimes used, the elliptical undulator (EPU) is the most successful device for the production of circularly polarized synchrotron radiation. In an EPU, the magnetic field vector rotates as a particle passes through the device, causing the particle to spiral about a central axis. Both electromagnetic and permanent magnet versions have been developed. Permanent magnet EPUs consist of 4 banks of magnets – two on top and two below (**Figure 4**).

The peak energy of the undulator output is changed by varying the vertical separation between the magnet assemblies, a so-called 'gap scan', while the polarization is varied by changing the relative positions (phases) of adjacent rows of magnets – a 'row scan'. In the case of the EPU on ALS beamline 4.0.1, the polarization can be changed from left to right circular polarization in a few seconds, and the peak energy can be varied as quickly as the monochromator scans [32].

Soft X-Ray Beamlines. In the soft x-ray region, beamlines use grazing incidence mirrors and gratings. In these geometries, the source polarization is almost completely preserved as it passes through the optics. For example, ALS beamline 4.0.1 employs an initial horizontally deflecting toroid (M1) at 2°, a plane pre-mirror (M3) at ~3°, a plane grating at variable glancing angle, a

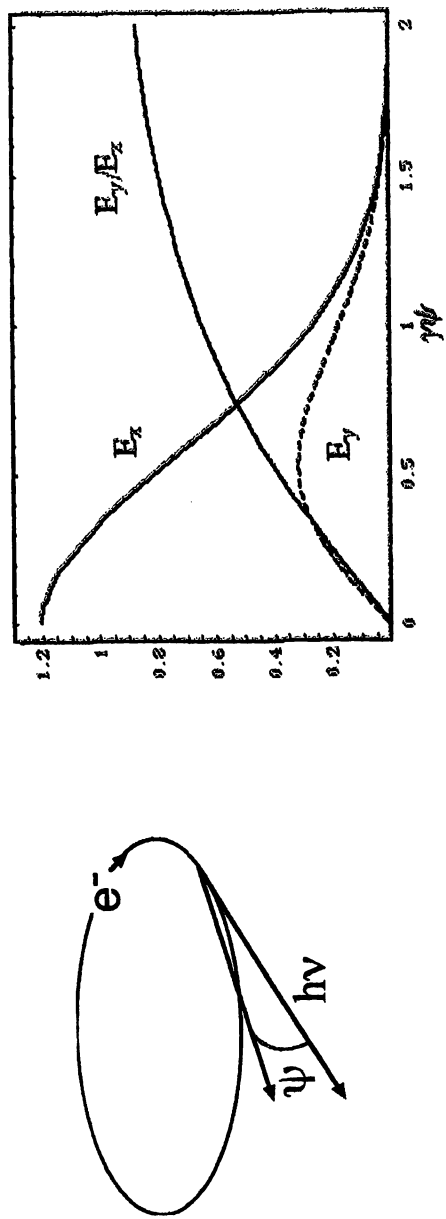

Publication Date: August 19, 2003 | doi: 10.1021/bk-2003-0858.ch020

In Paramagnetic Resonance of Metallobiomolecules; Telser, J.; ACS Symposium Series; American Chemical Society: Washington, DC, 2003.

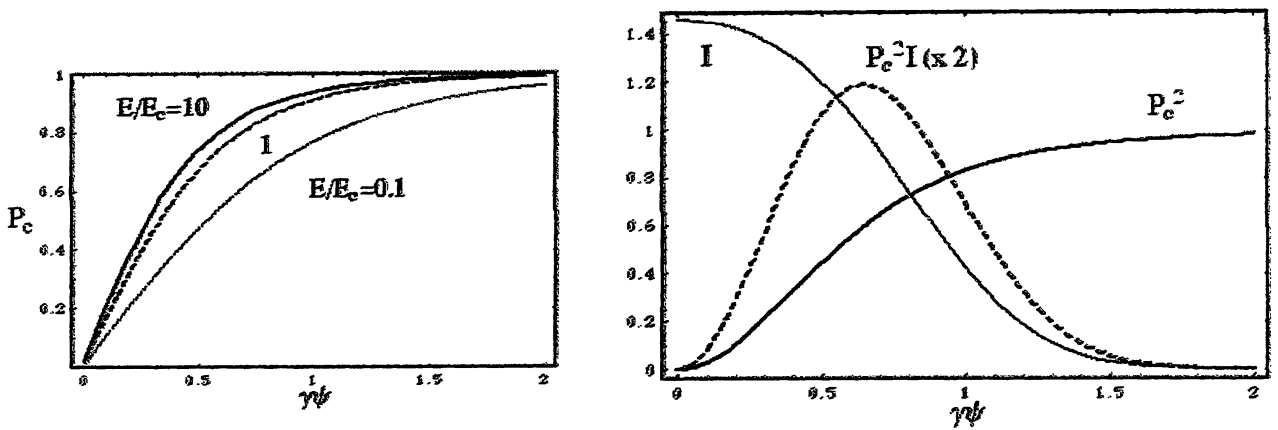

Figure 3 – (Top left) Definition of the observation angle ψ for synchrotron radiation vs. the orbital plane. (Top right) Amplitudes and ratio of x- and y-components of the electric field vs. vertical viewing angle (γψ). (Bottom left) Degree of circular polarization (P_c) as function of γψ □□□ ratio of photon energy to critical energy (E/E_0). (Bottom right) Tradeoff between flux (I) and polarization (P_c), and figure of merit ($P_c^2 I$).

Publication Date: August 19, 2003 | doi: 10.1021/bk-2003-0858.ch020

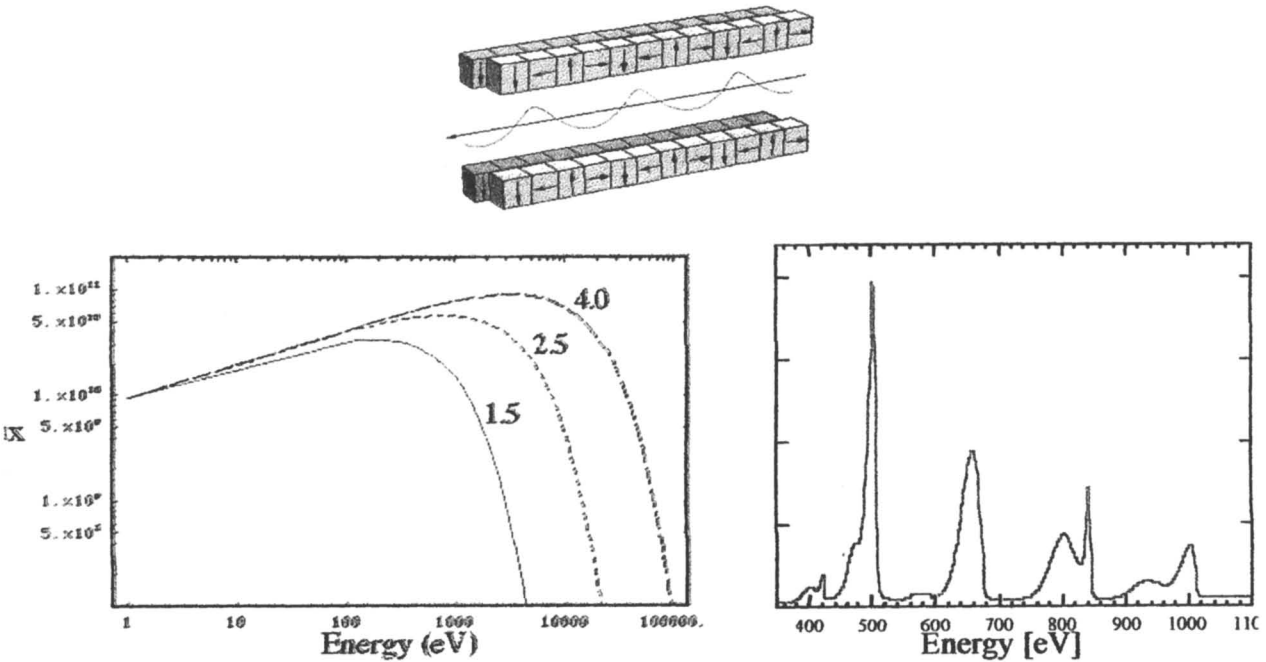

Figure 4 – (Top) Charged particle path through an EPU. Arrows represent field direction of permanent magnets. (Bottom left) Calculated spectra for different electron beam energies and bend magnet with 12.7 m bend radius (SSRL). Flux is in units of photons sec^{-1} mrad^{-1} mA^{-1} 0.1% bandwidth^{-1}. (Right) Measured output of ALS EPU.

In Paramagnetic Resonance of Metallobiomolecules; Telser, J.; ACS Symposium Series; American Chemical Society: Washington, DC, 2003.

cylindrical magnifying mirror (M4) at ~1°, and a final refocusing mirror (M5) at ~1° (**Figure 5**). This beamline provides ~10^{12} photons/sec with ΔE/E ~ 10,000 from 50-2000 eV [32].

Hard X-Ray Beamlines and Quarter Wave Plates. Hard x-ray applications employ crystal monochromators, and the effect of the crystal optics on the beam polarization can be considerable. A well-known phenomenon with visible light reflection is the so-called Brewster angle – the angle of incidence at which the electric field in the plane of incidence (π component) of a reflected beam is totally suppressed. This results in pure linear polarization along the out-of-plane or σ direction. The same phenomenon can occur with Bragg reflection from crystals. After all the hard work of producing perfect circular polarization from a hard x-ray EPU, the crystal optics can degrade the degree of circular polarization and in some cases produce pure horizontal polarization!

The solution is the same approach used with UV-visible MCD experiments: start with linear polarization and convert to circular polarization with a retarder, commonly a quarter wave plate. X-ray quarter wave plates exploit the birefringence of crystals for σ and π electric field components for geometries on or close to diffraction conditions. Although early work emphasized on-reflection Bragg or Laue geometries [24,28,33-35], some of the most popular x-ray quarter wave plates now operate in the off-Bragg transmission geometry. In this case, the crystal is adjusted to one of the wings of the Bragg reflection, at an angular deviation ΔΘ from the center of the rocking curve for Bragg angle Θ_B. The crystal planes are placed at a 45-degree angle to the incident polarization direction, to allow equal intensity for σ and π components of the electric field. The phase shift Δϕ, for a sufficiently large ΔΘ, depends on the difference in indices of refraction (n_σ - n_π), as well as the beam path *t* and wavelength λ [36]:

$$\Delta\phi = \frac{2\pi}{\lambda}(n_\sigma - n_\pi)t = -\left|\frac{r_e^2 F_h F_{\bar{h}}}{2\pi V^2}\frac{\lambda^3 \sin 2\theta_B}{\Delta\Theta}\right| t = A\frac{t}{\Delta\Theta}. \qquad (3)$$

where F_h and $F_{\bar{h}}$ are structure factors for h and $\bar{h}$ reflections, r_e is the classical electron radius, and V is the unit cell volume. By rocking a low-Z crystal such as diamond [37], Be [36], or LiF [38], from one side of the Bragg reflection to another, the polarization can be switched from lcp to rcp, with a $P_c > 90\%$. APS 4-ID-D is a specific beamline that uses such quarter wave plates (**Figure 6**) [39].

Magnetic Field and Temperature Control

The simplest samples for XMCD experiments are permanent magnets, such as the domains in disk storage devices. These samples can be magnetized separately from the XMCD measurement. For example, Stöhr and coworkers have used the XMCD effect to image magnetic domains in disk storage devices

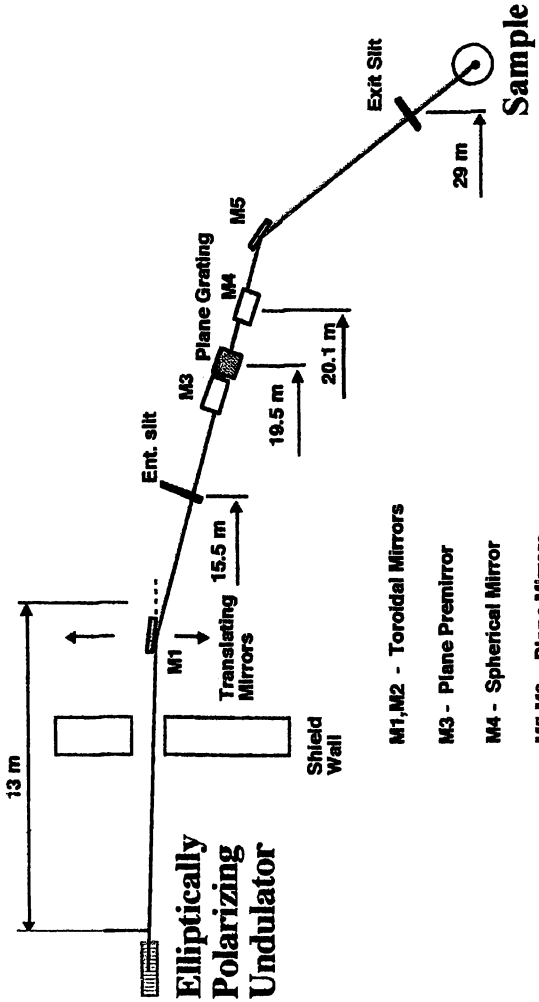

Figure 5 – ALS EPU beamline. M2 (mirror for 2nd undulator) is not yet installed.

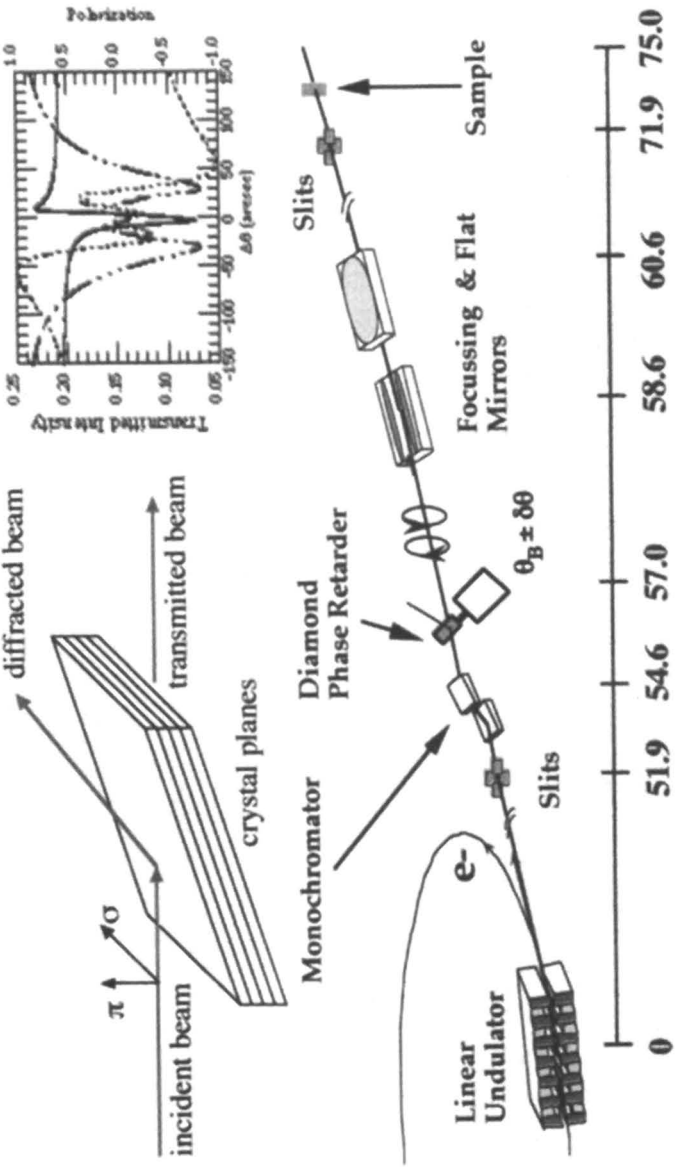

Figure 6 – (Top left) Bragg reflection and transmission geometries for x-ray quarter wave plates. (Top right) Phase shift difference for σ and π components as function of offset (Δθ) from Bragg condition. (Bottom) APS 4-ID-D, a hard x-ray line with quarter wave plates to provide circularly polarized x-rays [39].

[40]. Other groups have magnetized thin film samples *in situ* with a pulsed magnetic field, which is turned off during the experiment [41,42]. Ferromagnets are also easy to study, since only a small field need be applied. For example, the early measurements of Chen and coworkers used an external permanent magnet in close proximity to the Ni foil. The field was switched by manually reversing the external magnet [21]. NdFeB alloy permanent magnets are still used in some experiments to polarize the sample. Electromagnets make this process easier to automate, and several groups have used them in a variety of ways [43].

Superconducting magnets are required to achieve the highest magnetic fields. Our group has employed two different split coil designs. In one instrument, a 6 Tesla split coil is used, with a transverse gap between the coils [22,44]. This device has the advantage that full magnetization of the sample is achieved at 2-3 K, which is readily achieved with pumped ^{4}He cryostats. A temperature of ~0.5 K can be reached by using a ^{3}He inset with this device [45]. It has two limitations. First, the small gap limits the size of the Ge detector that can be introduced between the coils, hence we lose some solid angle of fluorescence collection. More important, the relatively large (31 Henry) inductance limits the rate at which the magnetic field can be reversed.

Our most recent instrument employs a ^{3}He-^{4}He dilution refrigerator, a split-coil 2-Tesla superconducting magnet system, and a 30-element windowless Ge fluorescence detector [46]. This device has a larger gap (8.25 cm), allowing insertion of the 30-element Ge detector close to the sample. It also has a low inductance winding (1.3 Henry), allowing field sweeps from +2T to –2 T in ~10 sec. Several layers of thermal shielding allow temperatures below 0.5 K to be reached routinely (**Figure 7**); in principle, 0.1 K should be possible.

Detection Methods

XMCD is essentially a measurement of relative absorption coefficients, hence all the detection methods used for conventional XAS can in principle be used. In practice, the three most important modes are transmission, fluorescence, and electron yield. As discussed long ago by Lee *et al.* [47], the optimum mode depends on the concentration and spatial distribution of the element under investigation, as well as fluorescence yields and matrix absorption coefficients. Since the factors involved in optimizing hard x-ray measurements are well known, we concentrate on the special requirements for MCD with soft x-rays.

Transmission is the simplest measurement, and it should be used whenever possible. The incident beam intensity (I_0) is often measured using the electron yield or photocurrent from a partially transmitting metal grid. The intensity after the sample (I) can be measured using a second grid, a solid metal plate, or a Si photodiode. Chen and coworkers have done careful transmission measurements of the XMCD of thin metal foils to check the accuracy of the sum rules [48], and with such samples transmission works beautifully. Unfortunately, in the soft x-

Publication Date: August 19, 2003 | doi: 10.1021/bk-2003-0858.ch020

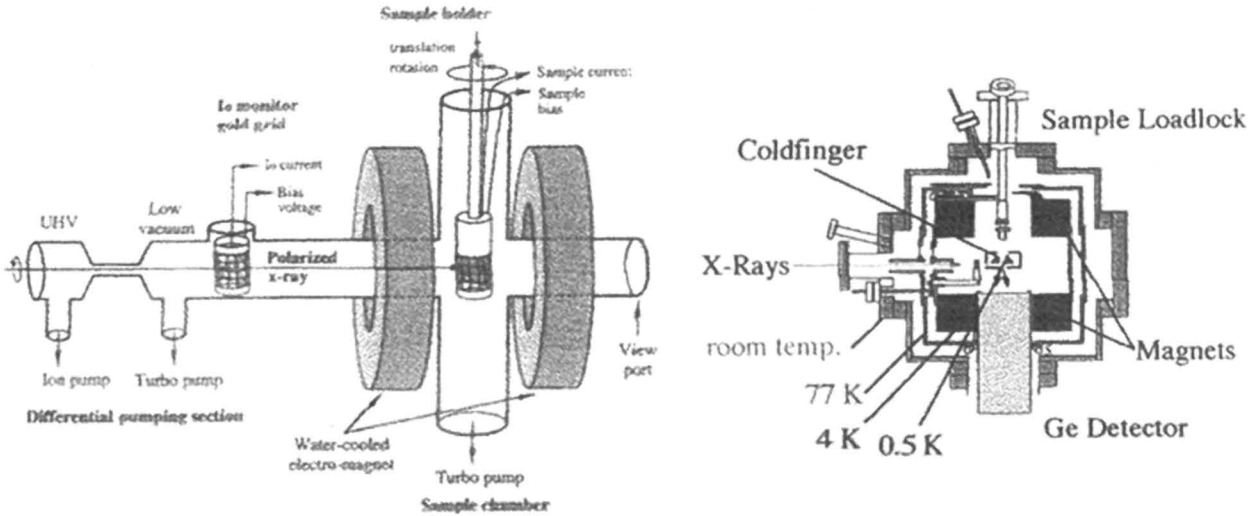

Figure 7 – (Left) A water-cooled electromagnet XMCD system for electron yield detection employed by Stöhr and coworkers [51]. (Right) Sketch of the dilution refrigerator XMCD instrument.

In Paramagnetic Resonance of Metallobiomolecules; Telser, J.; ACS Symposium Series; American Chemical Society: Washington, DC, 2003.

ray region, it is difficult to prepare metal complexes as homogeneous, pinhole-free samples with the required sub-micron thickness. As discussed by Stern [49] and Goulon [50], thick or porous samples will have suppressed absorption features due to 'leakage' effects, and consequently diminished XMCD amplitudes, especially if harmonics are present in the incident beam. Since the particle size of most samples is greater than the $1/e$ (<1μ) path-length, diluting the sample in a low Z powder or mull is of no use.

For concentrated inorganic samples, electron-based detection methods are preferred. One can either measure the electron yield directly with a channeltron electron multiplier (CEM), or indirectly as the photocurrent flowing to the sample from ground. Since electrons are emitted only from approximately the first 25-50 Å of sample, these approaches are very sensitive to oxidation or other surface reactivity. For very high cross sections, they can also suffer from saturation effects [51]. A problem for inorganic chemists is that many coordination complexes are poor conductors at the ~4 K temperature required for XMCD of paramagnets. To some extent, this can be overcome by (1) making very thin samples, (2) using a high collection voltage, (3) embedding the sample in a metallic grid, (4) pressing the sample particles into an indium foil, or (5) mixing the sample with a good conductor (Ag or graphite dust). The one generalization we can make from experience is that every sample is different.

Apart from S/N issues, electron methods may suffer from artifacts if magnetic field switching is used to measure the XMCD effect. The trajectories of emitted photoelectrons depend not only on their initial velocity, the applied voltage, and the geometry of collector placement, but also on the magnetic field. The apparent absorption cross section will vary if changing the field affects the fraction of photoelectrons that are accepted. Thus, electron-based XMCD measurements are best done with variable photon polarization.

Fluorescence yield might seem immune from magnetic field artifacts, but most detectors convert x-rays into electrons, and the resolution or gain can be influenced by a strong field. The detector sensitivity needs to be checked before varying the field for XMCD measurements or magnetization curves (**Figure 8**). Furthermore, as discussed by deGroot [52,53] and others [54], the fluorescence-detected excitation spectrum is not necessarily the same as the absorption spectrum, because the fluorescence yield can vary for different excited states. In extreme cases, a line can even be missing from the excitation spectrum (**Figure 8**) [54]! However, as noted by van Veenendaal and others, the effect is not usually that severe for XMCD [55,56]. They point out that, 'although in principle fluorescence yield is unequal to x-ray absorption, in the presence of a crystal field or of strong core-hole spin-orbit coupling fluorescence yield can be used to obtain ground state expectation values of L_z and S_z' (*vide infra*) [55]. From an experimentalist's point of view, a fluorescence-detected spectrum with known limitations is better than no spectrum at all.

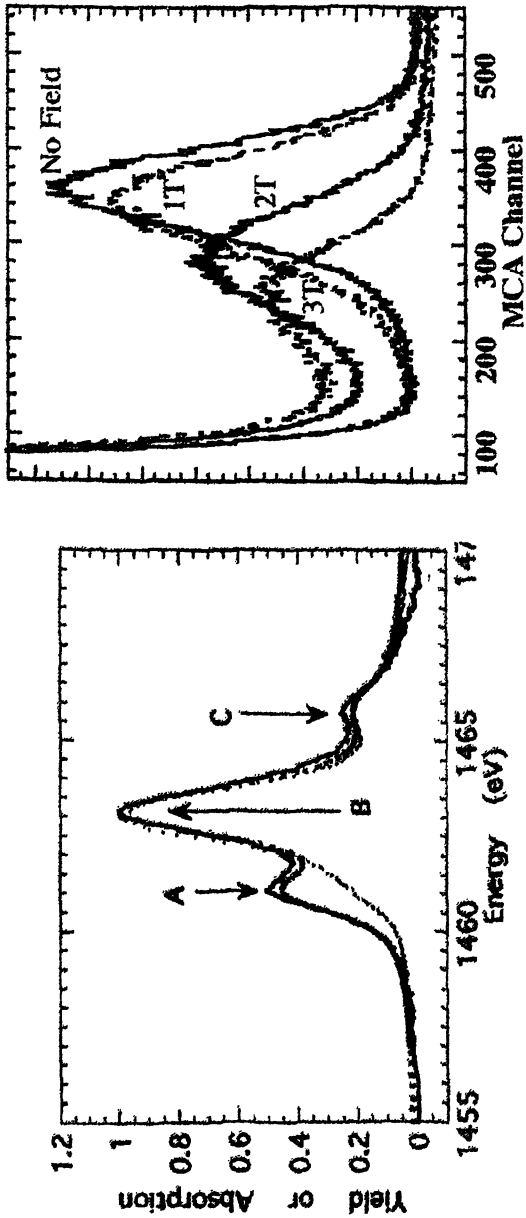

Figure 8 – (Left) Transmission (—), electron yield (+++), and fluorescence yield (···) spectra for a Tm film [54]. (Right) Field effects on Ge detector.

Finally, we should mention that even polarization-switched measurements suffer from potential artifacts. If the effective source point for left- and right-circularly polarized beams is slightly different, this can transform into an energy difference between the two beams at a given monochromator position. The slight mismatch will result in a derivative shaped contribution to the spectrum that is stronger for sharper features. Since this effect is independent of the applied field, one should check that there is indeed no XMCD effect in the absence of sample magnetization. (This presumes there is no 'natural' CD effect, but that is another story [57,58]).

Simplified Theory

"as simple as possible, but not simpler"
Albert Einstein

There are two common pictures used to describe the origin of the XMCD effect – Stöhr and Wu have described these as the '1-electron picture' and the 'configuration picture' [59]. A better name for the latter is the multiplet approach, because XMCD falls out naturally from ligand field multiplet theory. Below we compare the predictions of both pictures.

One-Electron Theory

A large fraction of the XMCD literature, especially papers involving magnetic thin film and metallic samples, uses the 1-electron model along with a 2-step approach to XMCD [59]. In this picture, the first step is to write the initial

Table 1 – Wave functions used in 1-electron model

1-Electron Label	$\|l\, s\, j\, m_j\rangle$ basis: m_l	$Y_l^{m_l}\Phi_{m_s}$
$^2p_{1/2}$	1/2	$\frac{1}{\sqrt{3}}(Y_1^0\alpha - \sqrt{2}Y_1^1\beta)$
	-1/2	$\frac{1}{\sqrt{3}}(\sqrt{2}Y_1^{-1}\alpha - Y_1^0\beta)$
$^2p_{3/2}$	3/2	$Y_1^1\alpha$
	1/2	$\frac{1}{\sqrt{3}}(\sqrt{2}\,Y_1^0\alpha + Y_1^1\beta)$
	-1/2	$\frac{1}{\sqrt{3}}(Y_1^{-1}\alpha + \sqrt{2}Y_1^0\beta)$
	-3/2	$Y_1^{-1}\beta$

orbitals for first transition metal L-edges as spin-orbit split $2p$ wave functions, as summarized below in **Table 1** [59].

The next step is to find expressions for the cross section matrix elements for transitions to various states with d symmetry. Assuming a constant radial matrix element R, Stöhr and Wu write these, citing Bethe and Salpeter [60], as:

$$\langle n', l+1, m_l+1 | P_1^{(1)} | n, l, m_l \rangle = \sqrt{\frac{(l+m_l+2)(l+m_l+1)}{2(2l+3)(2l+1)}}\, R \qquad (4)$$

and

$$\langle n', l+1, m_l-1 | P_{-1}^{(1)} | n, l, m_l \rangle = \sqrt{\frac{(l-m_l+2)(l-m_l+1)}{2(2l+3)(2l+1)}}\, R, \qquad (5)$$

where

$$P_1^{(1)} = \frac{1}{\sqrt{2}}(x+iy) = r\sqrt{\frac{4\pi}{3}}\, Y_1^1 \quad \text{and}$$

$$P_{-1}^{(1)} = \frac{1}{\sqrt{2}}(x-iy) = r\sqrt{\frac{4\pi}{3}}\, Y_1^{-1} \quad . \qquad (6)$$

These matrix elements are then evaluated for specific d-orbitals in spherical symmetry (Y_2^{ml}, β), and the 'oscillator strength' for different edge and polarization combinations is calculated by summing over m_l = -2, -1, 0, 1, and 2:

$$I_{L_3}^{+} = \sum_{i,f} \left| \langle f | P_1^{(1)} | i \rangle \right|^2 = \frac{1}{3}R^2,\ I_{L_3}^{-} = \frac{5}{9}R^2,\ I_{L_2}^{+} = \frac{1}{3}R^2, \text{ and } I_{L_2}^{-} = \frac{1}{9}R^2. \qquad (7)$$

Finally, the XMCD effect, for transitions solely to spin-down orbitals, is given by $\Delta I = I^+ - I^-$. For the L_3 edge, $\Delta I_{L3} = -(2/9)R^2$, while at the L_2 edge, $\Delta I_{L2} = +(2/9)R^2$. The key result from these calculations is that with lcp (using our 'optical' definition), *at the L_3 edge* the atom preferentially (5/8 of the time) emits *spin-up* electrons, while *at the L_2 edge* the atom preferentially (3/4 of the time) emits *spin-down* electrons.

The 1-electron model can also be used to explain the spin polarization of K-edges. In these cases, spin-orbit coupling of the final state p-electron is invoked [20,61]. However, as noted by Brouder and Hikam [62], at K-edges the relative amounts of spin-up and spin down states depend on the absorbing atom, the neighboring atoms, and the energy above threshold. Because spin-orbit coupling is much weaker, the degree of spin-polarization is typically 1% or less.

Band Theory and XANES XMCD

Once the spin polarization of the 'emitted' electron is established, the 1-electron model can be used to explain XMCD effects in both the XANES and EXAFS regions. In the 2-step model, the $p_{1/2}$ and $p_{3/2}$ shells are viewed as spin-polarized sources, and vacant spin-up and spin-down *3d* bands are viewed as spin-sensitive 'detectors' [63]. For example, if only spin down states are available, then the asymmetry, $(\sigma^+-\sigma^-)/(\sigma^++\sigma^-)$, at the L_2 edge should be a 50% effect, twice as large as at the L_3 edge (and opposite in sign). The simplest case, the rigid band 'Stoner model', is illustrated in **Figure 9**.

In a more sophisticated analysis, multiple scattering calculations using FEFF8 source code reproduced most of the Ni $L_{2,3}$ XMCD, including a controversial satellite 6 eV above the main resonance [64]. The latter peak was missing using a 13-atom cluster, but appeared in the 50-atom calculation. A lower energy feature at 3 eV was assigned to many body effects. The authors point out that no approach yet captures all the physics in the XMCD effect.

Scattering Theory and EXAFS XMCD

The EXAFS region is also sensitive to the spin polarization of emitted electrons – scattering by magnetic neighbors depends on the photoelectron polarization. When the neighboring atom is spin polarized, there will be an exchange contribution in addition to the Coulomb scattering potential. This will modify both the amplitude $f_0(\pi,k)$ and phase shift $\phi_0(k)$ for electron backscattering, so that the traditional formula for EXAFS for a single absorber-scatterer interaction requires modification. Schütz and coworkers proposed adding terms $f_c(\pi,k)$ and $\phi_c(k)$ for the magnetic backscattering amplitude and phase shift, scaled by the degree of photoelectron polarization σ_z [61]:

$$\chi(k) = \frac{e^{-2\sigma^2 k^2} e^{-R/\lambda}}{k R^2} |f(\pi,k)| \sin[2kR + \phi(k)] \qquad (8)$$

where:

$$f(\pi,k) = f_0(\pi,k) \pm \langle\sigma_z\rangle f_c(\pi,k) \text{ and } \phi(k) = \phi_0(k) \pm \sigma_z \phi_c(k) \; . \qquad (9)$$

The other terms have their conventional meaning: R is the absorber-scatterer distance, σ is the rms variation in R, k is the magnitude of the photoelectron wave vector, and λ is the photoelectron mean free path.

Ligand Field Multiplet Theory

Ligand field multiplet theory (LFMT) is a multi-electron viewpoint that describes the initial and final states as multiplets that are mixed and split by the

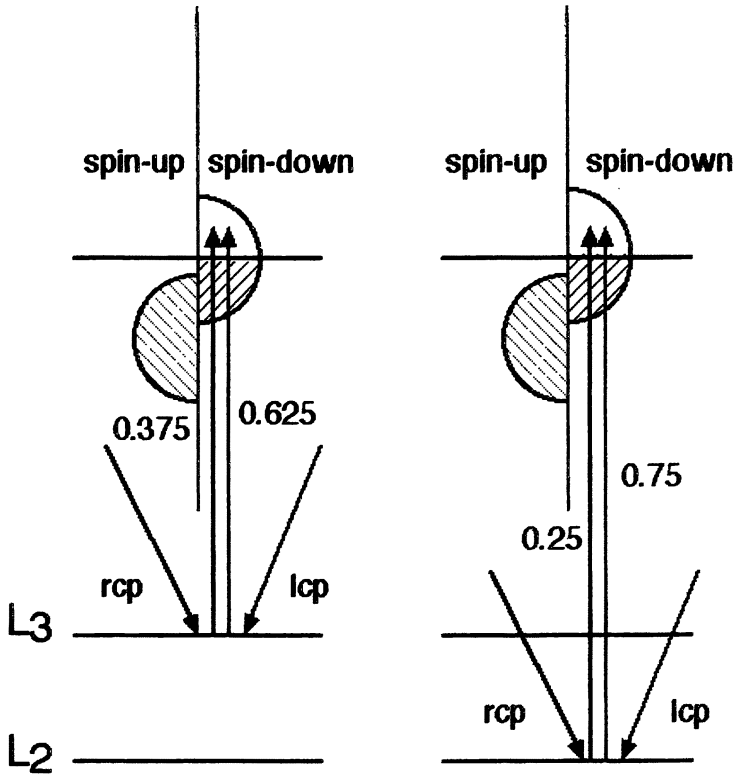

Figure 9 – Origin of L-edge XMCD in the 2-step model.

symmetry of the ligand field [65-69]. In this approach, the XMCD effect emerges naturally as a consequence of angular momentum selection rules. Spectra have been calculated for $3d^1$ through $3d^9$ systems with a range of crystal field and spin-orbital coupling strengths [70,71], so for many inorganic systems one can check beforehand to see the expected XMCD. Before discussing LFMT in detail, we illustrate the differences between 1-electron and multiplet approaches using the same $2p^63d^0 \rightarrow 2p^53d^1$ transition discussed previously.

In the L-S coupling scheme, the closed shell ground state for a d^0 system such as Ti^{4+} has zero spin and orbital angular momentum, $S = L = 0$, hence this is a ^1S term and the only level is $^1S_0$. For the $2p^53d^1$ final state configuration, there are 12 possible levels: the triplets – $^3P_{0,1,2}$, $^3D_{1,2,3}$, $^3F_{2,3,4}$, and the singlets – $^1P_1$, $^1D_2$, $^1F_3$. In the absence of any final state coupling, the ΔJ selection rule ($\Delta J = 0$, ± 1, no $0 \rightarrow 0$) allows only a single transition: $^1S_0 \rightarrow {}^1P_1$. Turning on the $2p$ spin-orbit interaction mixes the different *L-S* levels, and produces two accessible levels, a 'triplet' at $-(1/2)\xi_p$ and a 'singlet' at $+\xi_p$. The relative strengths are the familiar 2:1 ratio. So far, the results are the same as for the 1-electron picture.

LFMT predictions diverge from the 1-electron picture when interactions between partially filled $2p^5$ and $3d^N$ shells are included. These Coulomb and exchange interactions, described by the Slater-Condon parameters F^2, G^1, and G^3 [72], cause additional mixing of terms, so that the lowest energy (mostly triplet) level acquires $^1P_1$ character. Thus, even in spherical symmetry, LFMT predicts additional features that cannot be explained by 1-electron theory (**Figure**).

If one next turns on the ligand field portion of the theory, then J is no longer a 'good quantum number', and further mixing of levels occurs. In an O_h field, the symmetry of the initial state is A_1, the dipole operator is T_1, and final states must also have T_1 symmetry. It turns out there are 7 such levels – 4 derived from the $10Dq$ splitting of the 2 main peaks, and an additional 3 transitions not explained in 1-electron theory (**Figure 10**) [68]. (Branching from $O_3 \rightarrow O_h$ is explained in Butler [73]). These features are observed in d^0 systems such as KF, CaF_2, $FeTiO_3$ and ScF_3 [68], and their prediction and confirmation was one of the initial successes that helped confirm the utility of the LFMT approach.

Of course, for d^0 systems, there are no magnetic effects. What does LFMT have to say about the paramagnetic systems of interest in materials science and (bio)inorganic chemistry? For transition metal XMCD, the simplest case is the $2p^63d^9 \rightarrow 2p^53d^{10}$ transition seen with Cu(II) and Ni(I) complexes, as explicated in a classic paper by van der Laan and Thole [71]. They begin by writing the initial and final states of an atom in a magnetic field as $|\alpha JM\rangle$ and $|\alpha' J'M'\rangle$, where J and M are the total angular momentum and magnetic moment respectively, and α designates all other quantum numbers. They note that the temperature-dependent line strength is given by:

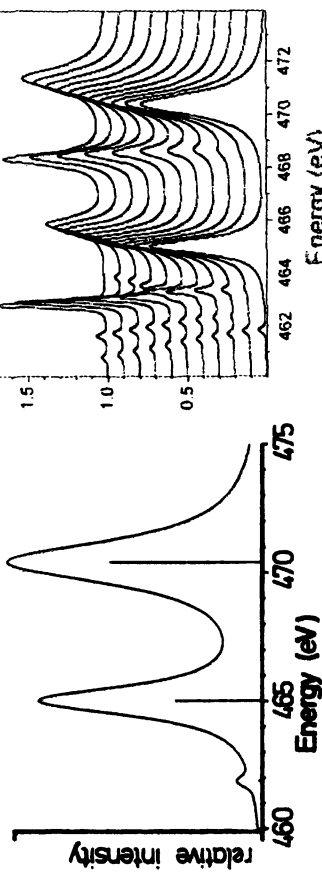

Figure 10 – $2p^6 3d^0 \rightarrow 2p^5 3d^1$ transitions for d^0 system (Ti^{4+}) in (left) O_3 symmetry with p-d *coupling [68], and (right) O_h ligand field and* p-d *coupling. 10*Dq *is 0 for lowest curve and increases to 3.0 eV for top curve.*

In Paramagnetic Resonance of Metallobiomolecules; Telser, J.;
ACS Symposium Series; American Chemical Society: Washington, DC, 2003.

$$\left\langle S^{q}_{\alpha J,\alpha' J'}\right\rangle = \left\langle A^{q}_{JJ'}\right\rangle \left|\left\langle \alpha J \left\| C^{(1)} \right\| \alpha' J' \right\rangle\right|^{2}, \qquad (10)$$

where the last factor is the line strength of the $\alpha J \rightarrow \alpha' J'$ transition, and the geometric factor $\left\langle A^{q}_{JJ'}\right\rangle$ distributes this intensity over the different $M \rightarrow M'$ transitions:

$$\left\langle A^{q}_{JJ'}\right\rangle = \left[\sum_{M}\begin{bmatrix} J & 1 & J' \\ M & q & M \end{bmatrix}^{2} e^{-M/\theta}\right] \Big/ \sum_{M} e^{-M/\theta} \qquad (11)$$

In the above equation θ is the reduced temperature, $\theta = kT/|g\mu_B|H$, and the squared term in the summation is a '3*j* symbol' [71]. Once the wave function is described in terms of *M* and *J*, the XMCD intensities at T = 0 derive from the angular momentum algebra contained in the *3j* symbol.

Life is simple in spherical symmetry. The initial d^9 ^2D term is split by spin-orbit coupling into $^2D_{3/2}$ and $^2D_{5/2}$ levels by the 3*d* spin-orbit interaction, and in a magnetic field; the latter is split by the Zeeman effect into 6 distinct states. At T = 0, there is only one allowed transition, $^2D_{5/2}$ (M_J = -5/2) → $^2D_{5/2}$ (M_J = -3/2), thus $\Delta M_J = q = +1$. This corresponds with absorption of lcp x-rays with our optical definition (**Figure 11**).

Of more interest to chemists is the effect of a ligand field on the energies and intensities of different transitions. For example, for Cu^{2+} in D_4 symmetry, the wave function can have B_1, A_1, B_2, and E irreducible representations [74]. Splitting by spin-orbit coupling and a magnetic field along the *z*-axis yields a Γ_8 ground state that is a mixture of |5/2,3/2>, |5/2,-5/2>, and |3/2,3/2> levels [71]. When the spin-orbit splitting is small compared to crystal field splittings, first order perturbation theory gives the ground state wave function as [71]:

$$|\Gamma_8> = |b_1> + \zeta_d/\Delta(b_2)|b_2> + (1/\sqrt{2})\,\zeta_d/\,\Delta(e)|e> \qquad (12)$$

The results of the van der Laan and Thole analysis are reproduced in **Table 2**. Note the major difference between LFMT and '2-step' predictions. In the absence of ground state spin-orbit coupling, LFMT predicts a branching ratio of 1 for *q* = -1 (a 100% XMCD effect at the L_2 edge). In contrast, 1-electron theory predicts at most a 50% asymmetry.

The complexity of XMCD spectra increases rapidly as (a) the number of *d*-electrons nears a half-filled shell, (b) charge-transfer effects require inclusion of multiple configurations, (c) lower symmetry requires inclusion of orientation dependence, and (d) zero field splittings complicate the magnetic field dependence. Since this is a primer and not an encyclopedia, we merely mention potential complications and point the interested reader toward the relevant literature.

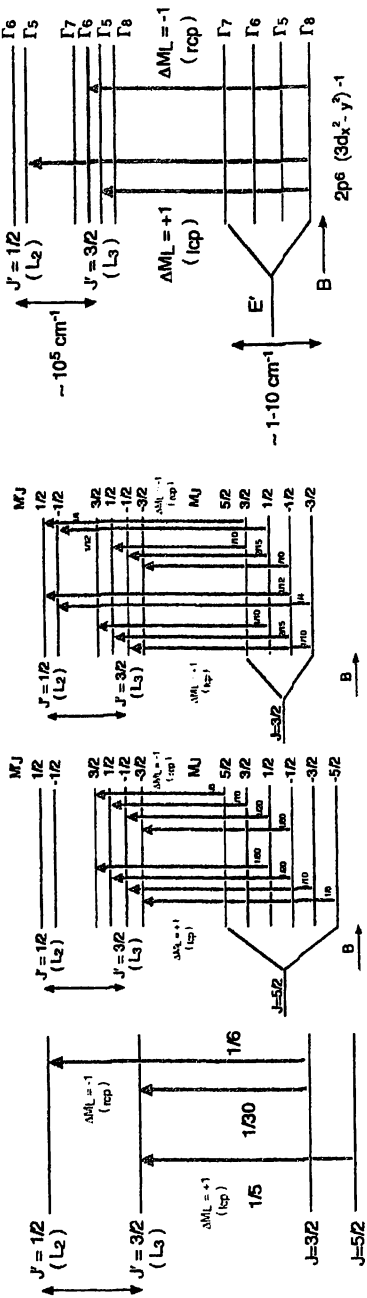

Figure 11 – XMCD transitions for atomic and molecular Cu(II). Fractions next to arrows are relative intensities. (Left) Dipole transitions in spherical symmetry [71]. (Middle) Left- and right-circularly polarized transitions for d^9 configuration in magnetic field. (Right) Ground state circularly polarized transitions for d^9 in C_4 symmetry (D_{4h} plus magnetic field).

In Paramagnetic Resonance of Metallobiomolecules; Telser, J.;
ACS Symposium Series; American Chemical Society: Washington, DC, 2003.

Table 2 – Line Strength and Branching Ratio for d^9 System with Γ_8 Character in C_4 Symmetry.

Dipole Excitation	Line Strength (P)	Branching Ratio (B)
isotropic	1/5	$[2+2\zeta_{3d}/\Delta(b_2) + \zeta_{3d}/\Delta(e)] / 3$
$q = +1$	$[1-2\zeta_{3d}/\Delta(b_2)]/10$	$[1-2\zeta_{3d}/\Delta(b_2) + 2\zeta_{3d}/\Delta(e)] / 3$
$q = -1$	$[1+2\zeta_{3d}/\Delta(b_2)]/10$	1
$q = 0$	$[\zeta_{3d}/\Delta(e)]^2/20$	1

First of all, the calculations become more complex towards the middle of the transition series. As noted by deGroot [75], there are 1512 possible final states for a $2p^5 3d^5$ final state (for example, a Mn^{3+} initial state)! Furthermore, in lower symmetry structures, additional parameters (*Ds*, *Dt*) are required to describe the ligand field, and the potential for artificially good simulations rises proportionally. Van der Laan has pointed out that in C_1 symmetry, the XMCD is a sum over three fundamental spectra, and that measurements in four different geometries are required [76]. Searle and van Elp have discussed how the XMCD can vary dramatically for different molecular orientations, especially when there is a zero field splitting comparable or larger than the applied Zeeman splitting [77]. Finally, if charge transfer is significant between the metal ion and the ligands (L), then two or more configurations (*e.g.* $3d^N$, $3d^{N+1}\underline{L}$) may be required to describe the electronic structure of both the initial and final states. Configuration interaction will add additional free parameters to the spectroscopic model. Given the potential complications to spectral simulation, it is fortunate that an alternate approach exists that requires far fewer assumptions – sum rule analysis.

Sum Rule Analysis

Sum rules are equations based on integrated spectra, and they allow derivation of valuable information without resort to simulation or fitting techniques. For example, most chemists are familiar with the Kuhn-Thomas sum rule, which states that the sum of oscillator strengths f_{no} is equal to the number of electrons N_e [78]:

$$\sum_n f_{n0} = N_e \qquad (13)$$

The first x-ray sum rule to consider states that the integrated intensity over particular absorption edges reflects the number of empty states with the appropriate symmetry for the transition [79]:

$$\int_{J_+ + J_-} (\mu_0 + \mu_1 + \mu_{-1})\, d\omega \propto \frac{4l + 2 - n}{2l + 1} P^2_{cl\,l} \qquad (14)$$

For $L_{2,3}$ edges, which have an initial p level, the transitions are primarily to states of d-symmetry, since the $2p \rightarrow 4s$ transitions are ~20-fold weaker than the $2p \rightarrow 3d$ transitions [80]. The decrease in the number of d-vacancies across the first transition series is nicely illustrated by comparing the white line intensities of the pure metals [51]. We have used this sum rule to quantify the amount of electron density transferred from copper to its ligands in blue copper proteins [81] and the Cu_A site, as well as the number of $3d$ vacancies in compounds with different Ni oxidation states [82].

For XMCD, the most important sum rules involve projections of the spin $\langle S_z \rangle$ and orbital $\langle L_z \rangle$ angular momentum of the absorbing species. In general terms:

$$\delta = \frac{\int_{J_+} (\mu_1 - \mu_{-1})\, d\omega - \frac{c+1}{c} \int_{J_-} (\mu_1 - \mu_{-1})\, d\omega}{\int_{J_+ + J_-} (\mu_0 + \mu_1 + \mu_{-1})\, d\omega} = \frac{l(l+1) - 2 - c(c+1)}{3c(4l + 2 - n)} \langle S_z \rangle \hbar + \alpha \langle T_z \rangle \hbar \qquad (15)$$

and

$$\rho = \frac{\int_{J_+ + J_-} (\mu_1 - \mu_{-1})\, d\omega}{\int_{J_+ + J_-} (\mu_0 + \mu_1 + \mu_{-1})\, d\omega} = \frac{1}{2} \frac{l(l+1) + 2 - c(c+1)}{l(l+1)(4l + 2 - n)} \langle L_z \rangle \hbar \qquad (16).$$

Stöhr and König have shown that the $\langle T_z \rangle$ angular term averages to zero in 'powder' samples [83], so this term in **Equation 15** can often be omitted. The quantities involved in sum rule analysis are illustrated graphically in **Figure 12**. Using these A, B, and C terms to represent the appropriate integrals, neglecting the $\langle T_z \rangle$ term, and assuming that $\mu_0 = (\mu_1 + \mu_{-1})/2$ [84], yields the following simple expressions for the sum rules:

$$\langle L_z \rangle = \frac{2(A + B)}{3C} n_h \qquad \langle S_z \rangle = \frac{A - 2B}{2C} n_h. \qquad (17)$$

The sum rules have been tested by comparison with experimental measurements [48,51] and theoretical calculations [85,86]; they are generally

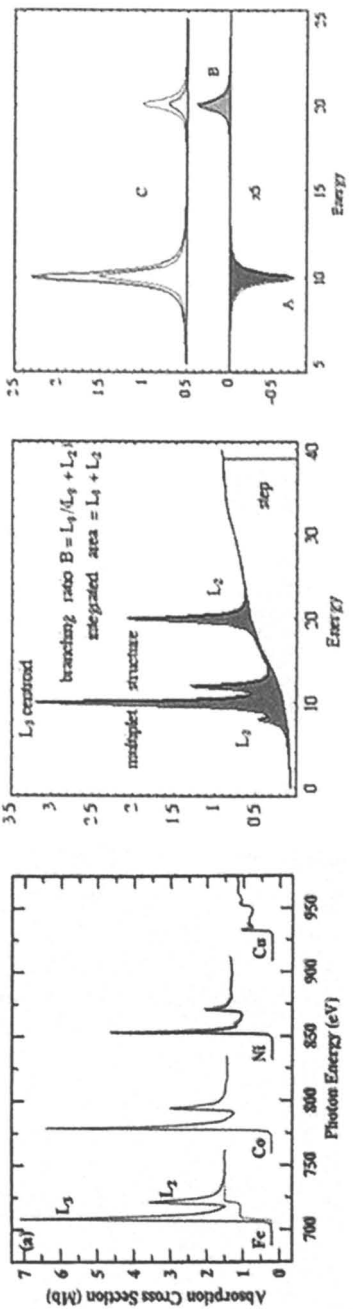

Figure 12 – (Left) White-line intensities of some first transition metals. Important quantities in hypothetical L-edge (middle) and XMCD (right) spectra. C is the average area under the absorption curves.

thought to be accurate within about 10%. Sainctavit, Arrio, and Brouder have done analytical calculations for Cu(II) in an octahedral ligand field that address the sum rule assumptions [87]. They found that at low temperature, the $\langle T_z \rangle$ term makes a large contribution to the spin sum rule and cannot be ignored. Others have shown that $\langle T_z \rangle$ can also be significant for other first transition metals, especially at lower symmetry surface sites [88].

Chemical Applications of XMCD

Deciphering Mixtures

Real world samples are often inhomogeneous. In some spectroscopic techniques, such as EPR, this is not a major problem – non-magnetic components do not give a signal, and overlapping spectra can be separated by exploiting different power saturation curves or by other methods. Inhomogeneity is more a problem for conventional x-ray spectroscopy, where chemical shifts are relatively small compared to natural line widths. XMCD provides an extra tool for separating magnetic and non-magnetic components in an x-ray spectrum, as well as for distinguishing components with different magnetic moments.

For example, in collaboration with David Grahame, we have studied the β*-subunit 'A-cluster' Ni site of *M. thermophila* ACDS protein [89]. This is presumably related to the active site for acetyl-CoA synthesis in the α subunit of carbon monoxide dehydrogenase/acetyl-CoA synthase (CODH/ACS) from *C. thermoaceticum*, where a recent crystal structure has revealed a unique Ni-Cu-Fe_4S_4 cluster (**Figure 13**) [90].

Both high spin (paramagnetic) and low-spin (diamagnetic) Ni(II) have been proposed as constituents of various Ni enzymes [91,92]. When we examined the Ni L-edge spectrum of one particular sample (that might have had some O_2 exposure), we observed a complex spectrum with at least three bands (**Figure 13**). The XMCD spectrum showed that the low and high energy features were magnetic, and most likely represented two components of a single high-spin Ni(II) spectrum. The central peak did not show an XMCD effect and most likely represented low-spin Ni(II). One hypothesis is that Ni occupies both 'external' sites in this particular protein. Our working hypothesis is that the low-spin Ni occupies the more square planar 'M_b' site, while the high-spin Ni occupies the more tetrahedral 'M_a site'. The observed heterogeneity would be hard to infer from the K-edge XANES or EXAFS alone.

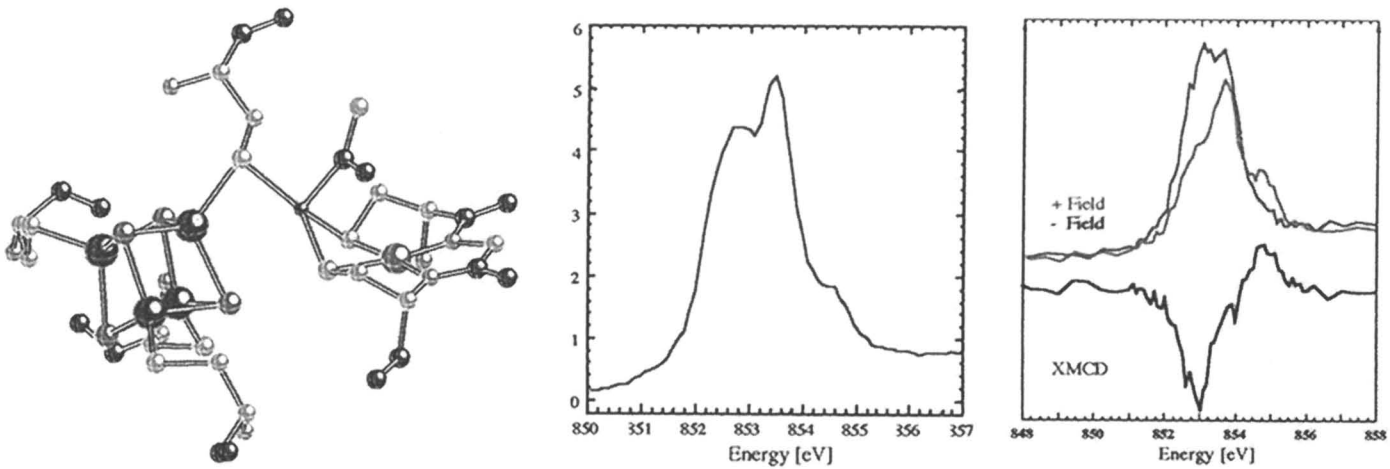

Figure 13 – (Left) Proposed structure for the 'A-cluster' of M. thermophila *ACDS protein [90]. (Middle) Ni L-edge absorption spectrum for the β*-subunit A-cluster. (Right) XMCD spectrum for the same sample.*

In Paramagnetic Resonance of Metallobiomolecules; Telser, J.; ACS Symposium Series; American Chemical Society: Washington, DC, 2003.

Magnetic Coupling

Since the sign of the XMCD effect reveals the net spin orientation for a given element or oxidation state, this technique can probe the interaction between different species in magnetically coupled systems. The easiest cases to study are interactions between different elements, because the edges are usually well separated in energy. The first such application was a temperature dependent XMCD study of $Fe_3Gd_3O_{12}$ [93]. At room temperature, the primary Fe XMCD signal was negative, while the Gd signal was positive. This indicated that the bulk magnetic moment was dominated by the contribution from the Fe spins, and that the Gd was antiferromagnetically coupled to the Fe. At low temperature, the Gd M_3 edge showed a strong negative XMCD, indicating that the Gd moment became the dominant factor, while positive Fe L_3 edge XMCD again indicated antiferromagnetic coupling.

In collaboration with Edward Solomon and Kenneth Karlin and their co-workers, we have used XMCD to observe antiferromagnetic coupling between Fe and Cu in Karlin's cytochrome oxidase model, $[(F_8\text{-TPP})Fe^{III}\text{-}(O^{2-})\text{-}Cu^{II}(TMPA)]^+$, **Figure 14**. This is a total spin $S_t = 2$ system resulting from antiferromagnetic coupling between $S = 5/2$ high-spin Fe(III) and $S = 1/2$ Cu(II). As expected, Fe and Cu have opposite sign XMCD.

XMCD analysis can also be used to study the magnetic coupling in mixed valence of the same element, provided there is a useful chemical shift between different oxidation states. Our long-term goal is to use XMCD for interpreting the spectra of complex clusters, such as the M center in nitrogenase [94] and the oxygen-evolving complex (OEC) of photosystem II [95]. As a model for the latter problem, we studied the C_{15}-carboxylate derivative of a 'single-molecule magnet' $Mn_{12}O_{12}(O_2CR)_{16}(H_2O)_4$ cluster system from George Christou's lab [96], **Figure 15**. The spectrum shows a strong bipolar signal at both L_3 and L_2 edges. The negative XMCD at the L_3 edge is assigned primarily to the set of 8 Mn(III) ions that are ferromagnetically coupled, while the positive signal at higher energy corresponds mostly to the central cube of 4 Mn(IV) ions whose magnetic moments are predominantly opposite to the net magnetization. A more detailed analysis with LFMT simulations is still in progress.

More complex XMCD is seen for $[Fe_2(II,III)(bpmp)(\mu\text{-}O_2CC_2H_5)_2][BPh_4]_2$ [97]. In a 6 T field, both signals are negative, indicating that the spins are mostly parallel and that the Zeeman interaction overwhelms both the zero field splittings D and the exchange interaction J_{AB}. The observed XMCD was ~34% of the effect expected for two independent and totally oriented Fe(II) and Fe(III) ions, indicating that the temperature and field were not sufficient to achieve total spin alignment. In a weaker field (1 T), the Fe(II) XMCD became quite weak.

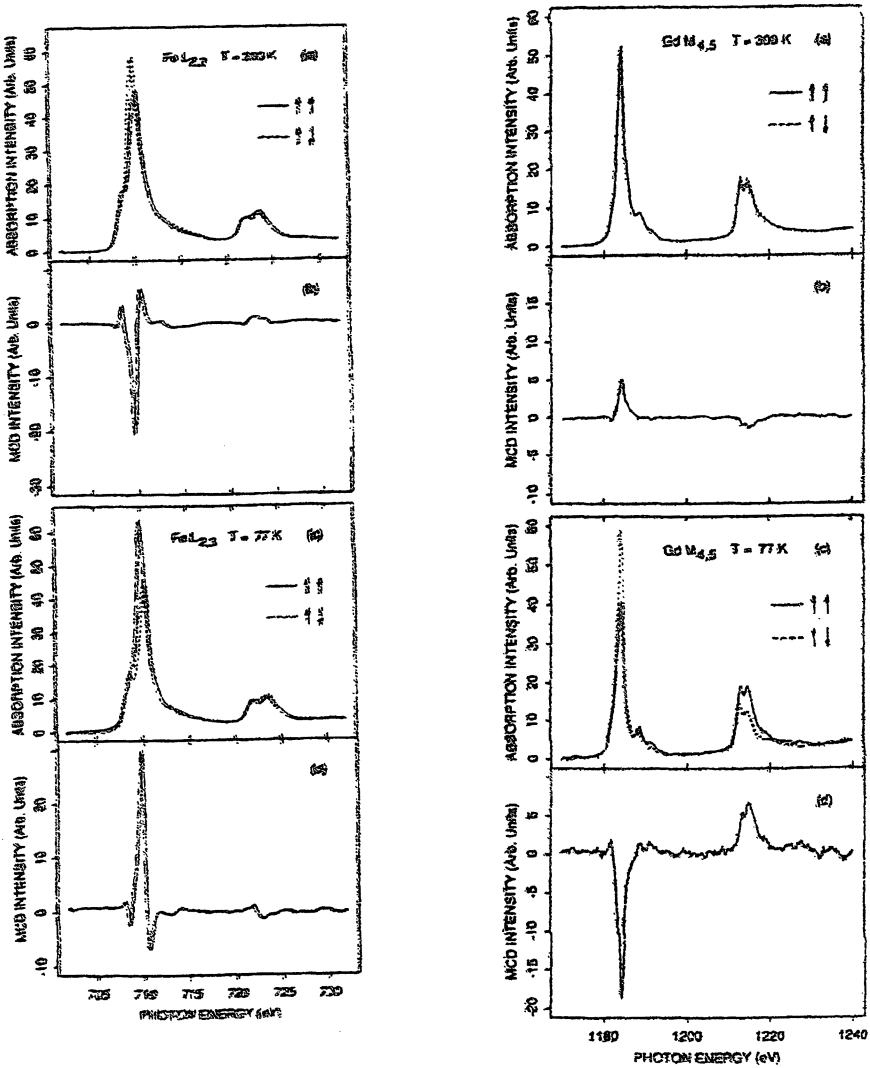

Figure 14 – Fe L-edge (left) and Gd M-edge (middle) XMCD spectra of $Fe_3Gd_3O_{12}$ reported by Rudolf et al. [93]. (Right) XMCD for (top) Cu and

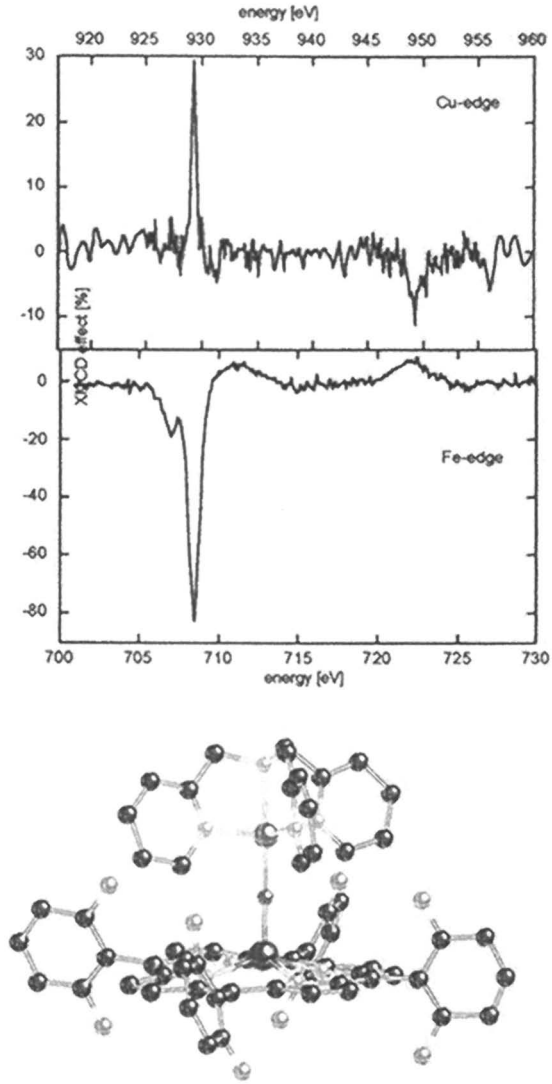

(bottom) Fe XMCD for Karlin's FeCu complex (structure shown below).

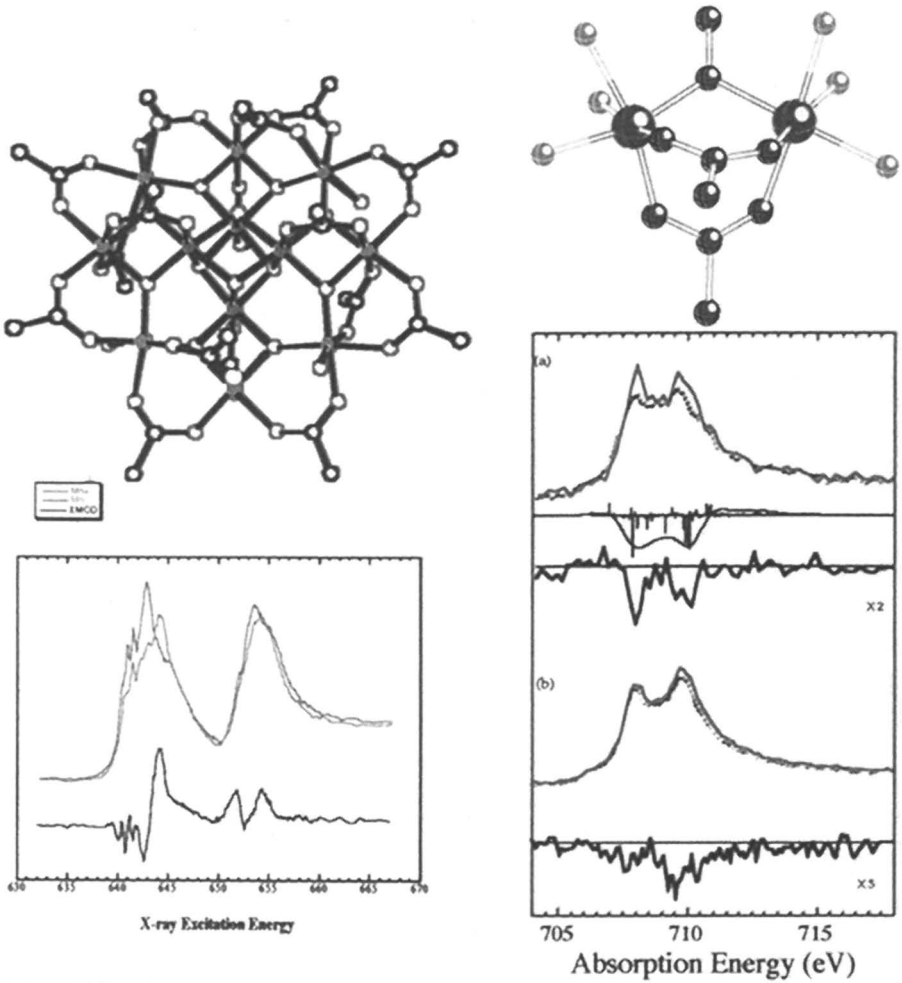

Figure 15 – XMCD of magnetically coupled systems of same element. (Left) XMCD for $[Mn_{12}(III,IV]$ complex in 6 T field. Spectra with lcp (- - -) and rcp (—) and XMCD. (Middle) XMCD spectra for $[Fe_2(III,II)(bpmp)(\mu\text{-}O_2CC_2H_5)_2][BPh_4]_2$ in different fields. (a) Top: spectra with lcp (- - -) and rcp

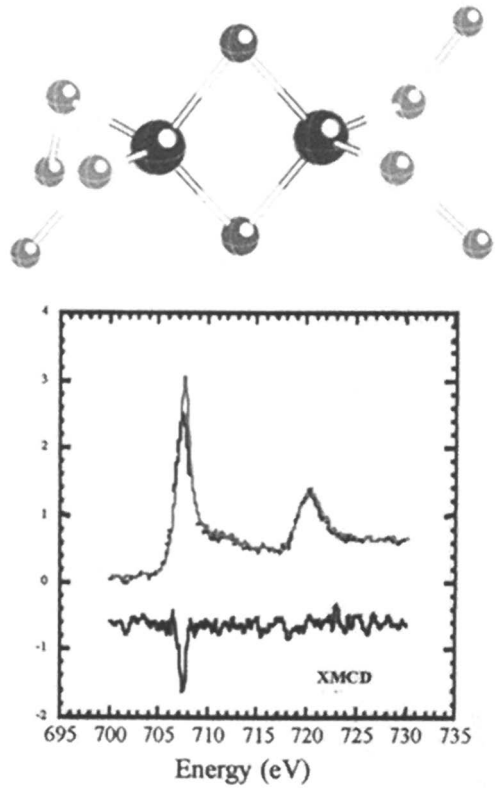

(—); middle: sum of calculated XMCD for Fe(II) and Fe(III); bottom: experimental XMCD (b) XMCD at 1 T: spectra with lcp (- - -) and rcp (—) and XMCD spectrum [97]. (Right) Fe(II)Fe(III) 2Fe ferredoxin and XMCD at 6 T.

Neglecting zero field splittings, the antiferromagnetically coupled Fe(II) should eventually have a positive XMCD at a sufficiently weak magnetic field.

One of the most difficult systems we have encountered is the 'simple' S = 1/2 Fe(II)Fe(III) site encountered in reduced 2Fe ferredoxins. Subtraction of a reduced (S = 2) Fe(II) rubredoxin (Rd) XMCD signal from the oxidized S = 5/2 Fe(III) Rd spectrum yields a bipolar spectrum distinctly different from the experimental spectrum (**Figure 15**). At least two factors complicate this naïve analysis. First, Mössbauer data show that the covalency of Fe in the binuclear site is higher than in mononuclear Rd centers, and assuming a proportionality between isomer shift and L-edge shift, smaller x-ray shifts are expected. Second, one must consider the spectra from all the possible M_S states that give rise to the total S = 1/2. Not only is there a contribution from $M_{Fe(III)} = 5/2 + M_{Fe(II)} = -2$, but there are 4 other combinations (3/2, -1; 1/2,0; -1/2,1; -3/2,2) weighted in proportion to their Clebsch-Gordan coefficients [98].

Magnetic Moments from Sum Rule Analysis

Element specific magnetic spin moments have been one of the major applications of XMCD. Thanks to the 'charge', 'spin', and 'orbital sum rules', simple integration of properly normalized spectra can reveal the number of vacancies and the magnetic moments. The first bioinorganic application of XMCD sum rule analysis involved the 'blue Cu' site in plastocyanin. Application of the orbital sum rule yielded a Cu 3d specific $\langle L_z \rangle$ of ~0.07 $\hbar$ and $\langle S_z \rangle$ of ~0.18 $\hbar$ per Cu, both within 15% of values derived from SCF-Xα-SW calculations (**Figure 16**) [99]. Similar analyses are underway on Ni complexes (**Figure 16**).

Element-Specific Magnetization Curves

The field and temperature dependence of the XMCD effect yield information about the magnetization of a sample that can be interpreted independently of 1-electron or LFMT models. The advantage of x-rays over optical techniques such as the Kerr effect is that each element can be probed separately. An important technological application has been the study of the magnetization of different elements in magnetic multilayers, such as the 'spin-valve' heads used in modern high-density read heads [100]. These devices employ the giant magnetoresistance (GMR) effect to produce a large change in electrical current from a small change in applied field, thus allowing higher density information storage. We remind the reader that the magnetization of ferromagnetic samples can depend not only on temperature and the current applied field, but also on its previous values; in other words, samples can exhibit 'hysteresis' [101].

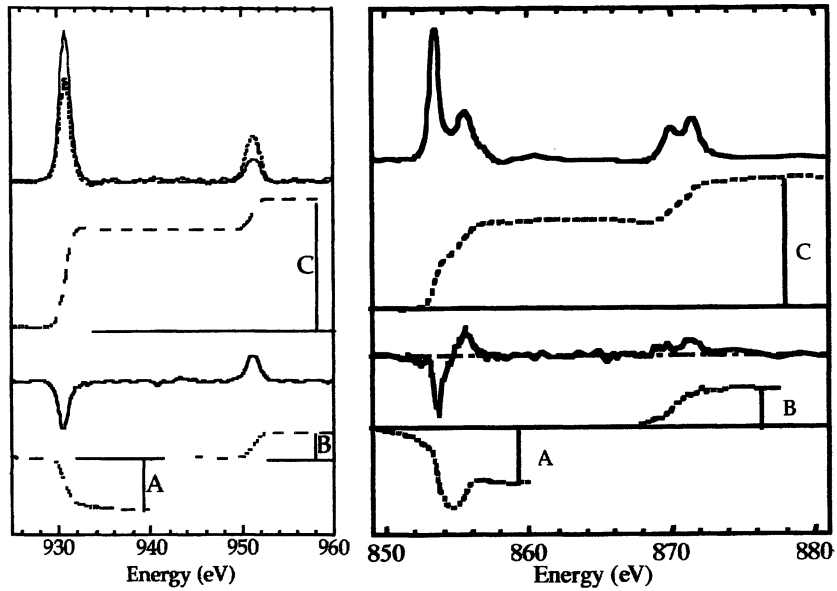

Figure 16 – (Left) XMCD spectra and sum rule integrations for the blue Cu site in plastocyanin. (Right) Absorption and XMCD spectra and sum rule integrations for the Ni(II) site in Ni-doped MgO.

For example, scientists at ESRF have studied a model trilayer system consisting of a (soft) 50 Å $Ni_{80}Fe_{50}$ layer, a variable thickness metallic Cu spacer, and a (hard) 50 Å Co layer, using fluorescence detected XMCD at the Ni and Co L_3 edges. With a thin (60 Å) Cu spacer and a slowly changing applied field, both Ni and Co reverse magnetization with the same coercive field, showing that the layers are strongly ferromagnetically coupled. With a thicker (100 Å) Cu spacer, the $Ni_{80}Fe_{50}$ layer requires a much smaller coercive field – the magnetic layers have become decoupled. By employing a pump-probe technique, the authors were able to observe the dynamics of the magnetization process on a nanosecond time scale [102].

For the paramagnets of interest in (bio)inorganic chemistry, the simplest model for the magnetization of N interacting atoms in volume V is given by $M = M_0 B(x,J)$, where M_0 is the saturation magnetization, $x = (g\mu_B H)/(kT)$ and $B(x,J)$ is the Brillouin function:

$$B(x,J) = \frac{2J+1}{2J}\coth\left(\frac{2J+1}{2J}x\right) - \frac{1}{2J}\coth\left(\frac{1}{2J}x\right) \quad \textbf{(18)}$$

which reduces to XMCD ~ $\tanh[(g\mu_B H)/(kT)]$ for S = 1/2 systems with no orbital moment [101]. The curves in **Figure 17** illustrate the potential of XMCD magnetization curves as a characterization tool separate from sum rule analysis and multiplet simulations. Magnetization curves should be especially useful for the analysis of mixtures, where different uncoupled species might magnetize at different rates. Of course, as noted by Pavel and Solomon [103], systems with zero field splittings such as Fe(II) can exhibit far more complex magnetization curves. Only recently has the quality of magnetization curves improved enough to warrant a more sophisticated analysis.

Electronic Structure

In UV-visible spectroscopy, MCD is often used to bring out detail in absorption spectra that are otherwise broad and featureless. L-edge XMCD can be used in the same manner. For example, the L-edge spectra of V(III) complexes are relatively uninformative, and can be modeled by a wide set of ligand field parameters. In contrast, the XMCD spectra contain a wealth of structure that puts additional constraints on any LFMT simulation (**Figure 18**).

XMCD can also help to distinguish $p \rightarrow d$ transitions from those that are primarily charge-transfer. In **Figure 18**, we show recent XMCD spectra for a Ni(I) complex from Charles Riordan's lab. As expected for a d^9 system, there is a strong signal at the L_3 edge, and the XMCD approaches a 100% effect at the L_2 edge. In contrast, a feature near 856 eV has almost no dichroism. We attribute the latter to a charge-transfer transition to an empty π^* orbital. DFT calculations are being done with Jorge Rodriguez to quantify these assignments.

Publication Date: August 19, 2003 | doi: 10.1021/bk-2003-0858.ch020

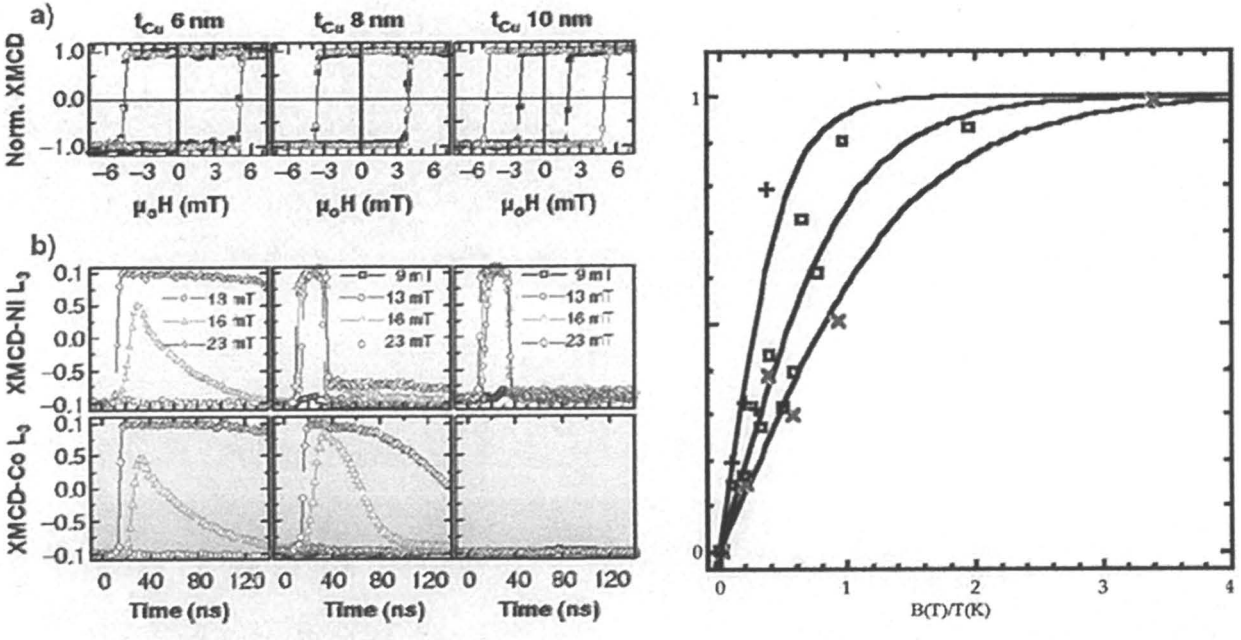

Figure 17 – (Left, top) XMCD magnetization curves obtained on the $Ni_{80}Fe_{20}$/Cu/Co trilayer system. Ni XMCD - filled circles, Co XMCD - open circles. (Left, bottom) Time dependence of Co and Ni magnetization. (Right) XMCD magnetization curves for Cu(II) in plastocyanin (x x x), compared with Ni(II) (□ □ □) and Mn(II) (+ + +) doped into MgO.

In Paramagnetic Resonance of Metallobiomolecules; Telser, J.; ACS Symposium Series; American Chemical Society: Washington, DC, 2003.

Publication Date: August 19, 2003 | doi: 10.1021/bk-2003-0858.ch020

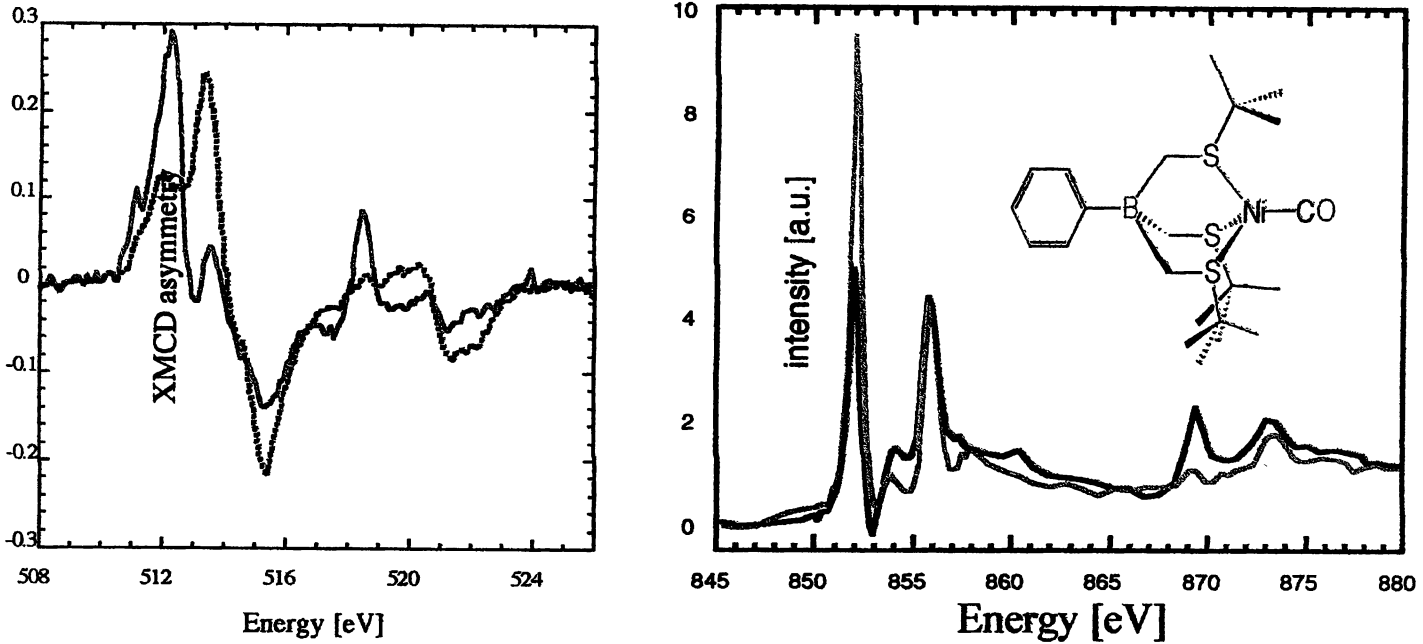

Figure 18 – (Left) XMCD for V(II) (—) and V(III) (···) Complexes. (Right) XMCD for Riordan's Ni(I)CO complex (structure shown in inset).

In Paramagnetic Resonance of Metallobiomolecules; Telser, J.; ACS Symposium Series; American Chemical Society: Washington, DC, 2003.

Summary – A Dose of Reality

'caveat emptor'

Few would argue that XMCD spectra, in principle, contain a wealth of information. As circularly polarized beamlines proliferate worldwide, access to and conduct of these measurements should become significantly easier. In ideal cases, XMCD should be able to reveal (a) the distribution of spin and orbital angular momentum in transition metal complexes (from sum rule analysis), (b) the strength of magnetic coupling between different centers (from the field dependence), and (c) the total magnetic moment (from the magnetization curve). In practice, intelligent use of the technique requires some caution.

For example, for systems more complicated than d^9 ions, the XMCD effect at a given edge is often bipolar or even more complex (see the calculations of van der Laan and Thole [70]). For the analysis of coupled systems, one is often faced with the question – is the XMCD bipolar because of antiferromagnetically coupled ions, or because of side lobes in a single component spectrum? In the extreme cases of Fe-S clusters, it seems that individual features can completely overlap, leaving a relatively featureless XMCD with multiple interpretations.

Experimental artifacts are also a concern, particularly radiation damage. Many samples are photoreduced in seconds on modern beamlines, and precautions such as sample motion or rapid scanning are often essential. Other potential problems include surface oxidation of reactive samples, beam heating at cryogenic temperatures, and surface anisotropy of magnetic properties. As discussed above, each detection scheme has the potential for mistakes as well.

Despite the potential difficulties, XMCD opens a window into electronic and magnetic structure and provides information that is often difficult to obtain by other techniques. For well-chosen problems, it should become a significant tool for the inorganic and bioinorganic communities.

Acknowledgements

'it takes a village ...'
African proverb

Our XMCD work has been made possible by generous support from the NSF (BIR-9015323, BIR-9317942, and SMB-9107312), NIH (GM-44380), and the DOE Office of Biological and Environmental Research. The support staff at NSLS, SSRL, and the ALS were essential for successful measurements, as were the beamline scientists – George Meigs at NSLS U4-B, Jeff Moore at SSRL 8-2, and Elke Arenholz and Tony Young at ALS 4.0.1. The hard work of postdocs

(Simon George, Jan van Elp, Jie Chen, Gang Peng, Marie-Anne Arrio, Lisa Miller, Tobias Funk, and Hongxin Wang) and students (Jason Christiansen, Xin Wang, Craig Bryant, and Wei-wei Gu) is deeply appreciated. Finally, I thank C. T. Chen and Francesco Sette for help getting XMCD started at the NSLS 'Dragon' beamline, George Sawatzky for initial encouragement to try paramagnetic XMCD, and Frank deGroot for a long and patient collaboration.

References

[1.] Born, M.; Wolf, E. Principles of Optics; Fifth ed.; Macmillan: New York, 1974.
[2.] Feynman, R. P.; Leighton, R. B.; Sands, M. The Feynman Lectures on Physics; Addison-Wesley: Reading, 1963; Vol. 1.
[3.] Kliger, D. S.; Lewis, J. W.; Randall, C. E. Polarized Light in Optics and Spectroscopy; Academic Press: San Diego, 1990.
[4.] Huygens, C. Traité de la lumière Leiden, 1690.
[5.] Maulus, É. L. Bul. Sc. Soc. Phil., **1809**, 1.
[6.] Newton, I. Opticks: or, a treatise of the reflexions, refractions, inflexions and colours of light.; S. Smith and B. Walford: London, 1704.
[7.] Fresnel, A. Oeuvres complètes; Imprimerie Imperiale: Paris, 1866.
[8.] Faraday, M. Experimental Research London, 1855; Vol. 3.
[9.] Faraday, M. Experimental Researches in Electricity; Green Lion Press, 2000.
[10.] Maxwell, J. C. A Treatise on Electricity and Magnetism Oxford, 1873.
[11.] Zeeman, P. Nature, **1897**, 55, 347.
[12.] Zeeman, P. Nobel Lecture, **1902**.
[13.] Röntgen, W. C. Nature, **1896**, 53, 274-276.
[14.] Forman, A. H. Phys. Rev., **1914**, 3, 306-313.
[15.] Forman, A. H. Phys. Rev., **1916**, 7, 119-124.
[16.] Erskine, J. L.; Stern, E. A. Phys. Rev. B, **1975**, 12, 5016.
[17.] Keller, E.; Stern, E. A., in EXAFS and Near Edge Structure III; Hodgson, K. O., Hedman, B. and Penner-Hahn, J. E., Ed.; Springer: Berlin, 1984, pp. 507-508.
[18.] Thole, B. T.; van der Laan, G.; Swatazky, G. A. Phys. Rev. Lett., **1985**, 55, 2086-2088.
[19.] van der Laan, G.; Thole, B. T.; Sawatzky, G. A.; Goedkoop, J. B.; Fuggle, J. C.; Esteva, J.-M.; Karnatak, R.; Remeika, J. P.; Dabkowska, H. A. Phys. Rev., **1986**, 34, 6529-6531.
[20.] Schütz, G.; Wagner, W.; Wilhelm, W.; Kienle, P.; Zeller, R.; Frahm, R.; Materlik, G. Phys. Rev. Lett., **1987**, 58, 737.
[21.] Chen, C. T.; Sette, F.; Ma, Y.-J.; Modesti, S. Phys. Rev. B, **1990**, 42, 7262-7265.

[22.] van Elp, J.; George, S. J.; Chen, J.; Peng, G.; Chen, C. T.; Tjeng, L. H.; Meigs, G.; Lin, H. J.; Zhou, Z. H.; Adams, M. W. W.; Searle, B. G.; Cramer, S. P. Proc. Nat. Acad. Sci. U. S. A., **1993**, 90, 9664-9667.
[23.] Goering, E.; Will, J.; Geissler, J.; Justen, M.; Weigand, F.; Schuetz, G. J. Alloys Compounds, **2001**, 328, 14-19.
[24.] Scalicky, P.; Malgrange, C. Acta Crys. A, **1972**, 28, 501-507.
[25.] Cox, J. A. M., Ph. D. Thesis, University of Leiden, 1954.
[26.] Huiskamp, W. J., Ph. D. Thesis, University of Leiden, 1958.
[27.] Reynolds, S. P. Space Science Rev., **2001**, 99:, 177-186.
[28.] Hart, M. Phil. Mag. B, **1978**, 38, 41-56.
[29.] Kim, K.-J. SPIE Proc., **1991**, 1548, 73-79.
[30.] Kim, K.-J. SPIE Proc., **1991**, 1345, 116.
[31.] Kitamura, H. Syn. Rad. News, **1992**, 5, 14-20.
[32.] Young, A. T.; Martynov, V.; Padmore, H. J. Elect. Spec. Rel. Phen., **1999**, 103, 885-889.
[33.] Golovchenko, J. A.; Kincaid, B. M.; Levesque, R. A.; Meixner, A. E.; Kaplan, D. R. Phys. Rev. Lett., **1986**, 57, 202-205.
[34.] Mills, D. M. Nucl. Inst. Meth. A, **1988**, 266, 531.
[35.] Mills, D. M., in Third Generation Hard X-Ray Synchrotron Radiation Sources: Source Properties, Optics, and Experimental Techniques; Mills, D. M., Ed.; John Wiley & Sons: New York, 2002, pp. 41-99.
[36.] Giles, C.; Malgrange, C.; Goulon, J.; Debergevin, F.; Vettier, C.; Fontaine, A.; Dartyge, E.; Pizzini, S.; Baudelet, F.; Freund, A. Rev. Sci. Inst., **1995**, 66, 1549-1553.
[37.] Varga, L.; C., G.; Zheng, Y. L.; Pizzini, S.; de Bergevin, F.; Fontaine, A.; Malgrange, C. J. Syn. Rad., **1999**, 6, 1125-1132.
[38.] Leitenberger, W.; Eisenschmidt, C.; Höche, H.-R. J. App. Crys., **1997**, 30, 164-170.
[39.] Freeland, J. W.; Lang, J. C.; Srajer, G.; Winarksi, R.; Shu, D.; Mills, D. M. Rev. Sci. Inst., **2002**, 73, 1408.
[40.] Stöhr, J.; Wu, Y.; Hermsmeier, B. D.; Samant, M. G.; Harp, G. R.; Koranda, S.; Dunham, D.; Tonner, B. P. Science, **1993**, 259, 658-661.
[41.] Tobin, J. G.; Waddill, G. D.; Jankowski, A. F.; Sterne, P. A.; Pappas, D. P. Phys. Rev. B, **1995**, 52, 6530-6541.
[42.] Dürr, H. A.; van der Laan, G.; Spanke, D.; Hillebrecht, F. U.; Brookes, N. B. Phys. Rev. B, **1997**, 56, 8156-8162.
[43.] Nakajima, R., Ph. D. Thesis, Stanford University, 1997.
[44.] George, S. J.; van Elp, J.; Chen, J.; Mitra-Kirtley, S.; Mullins, O. C.; Cramer, S. P., in Synchrotron Radiation in Biosciences; Chance, B., Ed.; Oxford University Press: Oxford, 1994.
[45.] Christiansen, J.; Peng, G.; A. T. Young, A. T.; LaCroix, L. B.; Solomon, E. I.; Cramer, S. P. Inorg. Chim. Acta, **1996**, 118, 229-232.

[46.] Bryant, C., M. S. Thesis, University of California, Davis, 1998.
[47.] Lee, P. A.; Citrin, P. H.; Eisenberger, P.; Kincaid, B. M. Rev. Mod. Phys., **1981**, 53, 769-806.
[48.] Chen, C. T.; Idzerda, Y. U.; Lin, H. J.; Smith, N. V.; Meigs, G.; Chaban, E.; Ho, G.; Pellegrin, E.; Sette, F. Phys. Rev. Lett., **1995**, 75, 152-155.
[49.] Stern, E. A.; Kim, K. Phys. Rev. B, **1981**, 23, 3781-3787.
[50.] Goulon, J.; Goulon-Ginet, C.; Cortes, R.; Dubois, J. M. J. Physique, **1982**, 43, 539-548.
[51.] Stöhr, J.; Nakajima, R. IBM J. Res. Develop., **1998**, 42, 73-88.
[52.] de Groot, F. M. F.; Arrio, M.-A.; Sainctavit, P.; Cartier, C.; Chen, C. T. Sol. State Comm., **1994**, 92, 991-995.
[53.] de Groot, F. M. F.; Arrio, M.-A.; Sainctavit, P.; C., C.; Chen, C. T. Phys. B, **1995**, 208-209, 84-86.
[54.] Pompa, M.; Flank, A. M.; Lagarde, P.; Rife, J. C.; Stekhin, I.; Nakazawa, M.; Ogasawara, H.; Kotani, A. Phys. Rev. B, **1997**, 56, 2267-2272.
[55.] van Veenendaal, M.; M. Goedkoop, J. B.; Thole, B. T. Phys. Rev. Lett., **1996**, 77, 1508-1511.
[56.] Goedkoop, J. B.; Brookes, N. B.; van Veenendaal, M.; Thole, B. T. J. Elec. Spect. Rel. Phenom., **1997**, 86, 143-150.
[57.] Carra, P.; Benoist, R. Phys. Rev. B, **2000**, 62, R7703-R7706.
[58.] Peacock, R. D.; Stewart, B. J. Phys. Chem. B, **2001**, 105, 351-360.
[59.] Stöhr, J.; Wu, Y., in New Directions in Research with Third-Generation Soft X-Ray Synchrotron Radiation Sources; Schlacter, A. S. and Wuilleumier, F. J., Ed.; Kluwer: Amsterdam, 1994, pp. 221-250.
[60.] Bethe, H. A.; Salpeter, E. E. Quantum Mechanics of One- and Two-Electron Atoms; Plenum: New York, 1977.
[61.] Schütz, G.; Fischer, P.; Goering, E.; Attenkofer, K.; Ahlers, D.; Rößl, W. Syn. Rad. News, **1997**, 10, 13-26.
[62.] Brouder, C.; Hikam, M. Phys. Rev. B, **1991**, 43, 3809-3820.
[63.] Since this review was written at World Series time, consider a baseball analogy. The L_2 edge can be likened to a pitcher is either left- or right-handed. The opposing batter can also be left- or right-handed ...
[64.] Nesvizhskii, A. I.; Ankudinov, A. L.; Rehr, J. J.; Baberschke, K. Phys. Rev. B, **2000**, 62, 15295-15298.
[65.] Yamaguchi, T.; Shibuya, S.; Suga, S.; Shin, S. J. Phys. C, **1982**, 15, 2641.
[66.] Thole, B. T.; van der Laan, G.; Butler, P. H. Chem. Phys. Lett., **1988**, 149, 295-299.
[67.] van der Laan, G.; Thole, B. T.; Sawatzky, G. A.; Verdaguer, M. Phys. Rev. B, **1988**, 37, 6587-6589.
[68.] de Groot, F. M. F.; Fuggle, J. C.; Thole, B. T.; Sawatzky, G. A. Phys. Rev. B, **1990**, 41, 928-937.

[69.] de Groot, F. M. F.; Fuggle, J. C.; Thole, B. T.; Sawatzky, G. A. Phys. Rev. B, **1990**, 42, 5459-5468.
[70.] van der Laan, G.; Thole, B. T. Phys. Rev. B, **1991**, 43, 13401-13411.
[71.] van der Laan, G.; Thole, B. T. Phys. Rev. B, **1990**, 42, 6670-6674.
[72.] Weissbluth, M. Atoms and Molecules; Plenum Press: New York, 1978.
[73.] Butler, P. H. Point Group Symmetry. Applications, Methods and Tables; Plenum: New York, 1981.
[74.] Cotton, F. A. Chemical Applications of Group Theory; 3rd ed.; Wiley-Interscience: New York, 1990.
[75.] de Groot, F. M. F.; Vogel, J., in, 2002, pp. in press.
[76.] van der Laan, G. J. Phys. Soc. Jap., **1994**, 63, 2393-2400.
[77.] van Elp, J.; Searle, B. G. J. Elect. Spec. Rel. Phenom., **1997**.
[78.] Atkins, P. W.; Friedman, R. S. Molecular Quantum Mechanics; Third ed.; Oxford University Press: Oxford, 1997.
[79.] Starace, A. F. Phys. Rev. B, **1972**, 5, 1773-1784.
[80.] Stöhr, J. J. Electron Spec. Rel. Phenom., **1995**, 75, 253-272.
[81.] George, S. J.; Lowery, M. D.; Solomon, E. I.; Cramer, S. P. J. Am. Chem. Soc., **1993**, 115, 2968-2969.
[82.] Wang, H.; Ge, P.; Riordan, C. G.; Brooker, S.; Woomer, C. G.; Collins, T.; Melendres, C.; Graudejus, O.; Bartlett, N.; Cramer, S. P. J. Phys. Chem. B, **1998**, 102, 8343-8346.
[83.] Stöhr, J.; Konig, H. Phys. Rev. Lett., **1995**, 75, 3748-3751.
[84.] Carra, P. Syn. Rad. News, **1992**, 5, 21-24.
[85.] Wu, R. Q.; Wang, D.; Freeman, A. J. Phys. Rev. Lett., **1993**, 71, 3581–3584.
[86.] Wu, R. Q.; Freeman, A. J. Phys. Rev. Lett., **1994**, 73, 1994–1997.
[87.] Sainctavit, P.; Arrio, M. A.; Brouder, C. Phys. Rev. B, **1995**, 52, 12766-12769.
[88.] Crocombette, J. T.; Thole, B. T.; Jollett, F. J. Phys.: Condens. Matter, **1996**, 8, 4095-4105.
[89.] Grahame, D. A.; Demoll, E. J. Biol. Chem., **1996**, 271, 8352-8358.
[90.] Doukov, T. I.; Iverson, T. M.; Seravelli, J.; Ragsdale, S. W.; Drennan, C. L. Science, **2002**, 298, 567-572.
[91.] Wang, H.; Ralston, C. Y.; Patil, D. S.; Jones, R. M.; Gu, W.; Verhagen, M.; Adams, M. W. W.; Ge, P.; Riordan, C.; Marganian, C. A.; Mascharak, P.; Kovacs, J.; Miller, C. G.; Collins, T. J.; Brooker, S.; Croucher, P. D.; Wang, K.; Stiefel, E. I.; Cramer, S. P. J. Am. Chem. Soc., **2000**, 122, 10544-10552.
[92.] Ralston, C. Y.; Wang, H.; Ragsdale, S. W.; Kumar, M.; Spangler, N. J.; Ludden, P. W.; Gu, W.; Jones, R. M.; Patil, D. S.; Cramer, S. P. J. Am. Chem. Soc., **2000**, 122, 10553-10560.
[93.] Rudolf, P.; Sette, F.; Tjeng, L. H.; Meigs, G.; Chen, C. T. J. Mag. Mag. Mat., **1992**, 109, 109-112.

[94.] Rees, D. C.; Howard, J. B. Curr. Op. Struct. Biol., **2000**, 4, 559-566.
[95.] Barber, J.; Anderson, J. M. Phil. Trans. Royal Soc. London B, **2002**, 357, 1325-1328.
[96.] Sessoli, R.; Tsai, H.-L.; Schake, A. R.; Wang, S.; Vincent, J. B.; Folting, K.; Gatteschi, D.; Christou, G.; Hendrickson, D. N. J. Am. Chem. Soc., **1993**, 115, 1804-1816.
[97.] Peng, G.; van Elp, J.; Jang, H.; Que, L.; Armstrong, W. H.; Cramer, S. P. J. Am. Chem. Soc., **1995**, 117, 2515-2519.
[98.] van Elp, J.; Peng, G.; Zhou, Z. H.; Mukund, S.; Adams, M. W. W. Phys. Rev. B, **1996**, 53, 2523-2527.
[99.] Wang, H.; Bryant, C.; Randall, D. W.; LaCroix, L. B.; Solomon, E. I.; LeGros, M.; Cramer, S. P. J. Phys. Chem. B, **1998**, 102, 8347-8349.
[100.] Tsang, C. H. F., R.E., Jr.; Lin, T.; Helm, D.E.; Gurney, B.A.; Williams, M.L. IBM J. Res. Dev., **1998**, 42, 103-116.
[101.] Cullity, B. D. Introduction to Magnetic Materials; Addison-Wesley: Reading, Mass., 1972.
[102.] Bonfim, M.; Ghiringhelli, G.; Montaigne, F.; Pizzini, S.; Brookes, N. B.; Petroff, F.; Vogel, J.; Camarero, J.; Fontaine, A. Phys. Rev. Lett., **2001**, 86, 3646-3649.
[103.] Pavel, E. G.; Solomon, E. I., in Spectroscopic Methods in Bioinorganic Chemistry; Solomon, E. I. and Hodgson, K. O., Ed.; American Chemical Society: Washington, D. C., 1998; Vol. 692, pp. 119-135.
[104.] Maruyama, H.; Suzuki, M.; Kawamura, N.; Ito, M.; Arakawa, E.; Kokubun, J.; Hirano, K.; Horie, K.; Uemura, S.; Hagiwara, K.; Mizumaki, M.; Goto, S.; Kitamura, H.; Namikawae, K.; Ishikawa, T. J. Syn. Rad., **1999**, 6, 1133-1137.